Current Based Automated Design of Realizable Metasurface Antennas With Arbitrary Pattern Constraints

Original
Current Based Automated Design of Realizable Metasurface Antennas With Arbitrary Pattern Constraints / Zucchi, Marcello; Vernì, Francesco; Righero, Marco; Vecchi, Giuseppe. - In: IEEE TRANSACTIONS ON ANTENNAS AND PROPAGATION. - ISSN 0018-926X. - STAMPA. - 71:6(2023), pp. 4888-4902. [10.1109/TAP.2023.3270715]

Publisher:
IEEE

Published
DOI:10.1109/TAP.2023.3270715

This article has been accepted for publication in IEEE Transactions on Antennas and Propagation. This is the author's version which has not been fully edited and content may change prior to final publication. Citation information: DOI 10.1109/TAP.2023.3270715

Current-Based Automated Design of Realizable Metasurface Antennas with Arbitrary Pattern Constraints

Marcello Zucchi, *Graduate Student Member, IEEE*, Francesco Vernì, *Member, IEEE*, Marco Righero, and Giuseppe Vecchi, *Fellow, IEEE*

***Abstract*—We present a 3D method to numerically design a realizable metasurface, which transforms a given incident field into a radiated field that satisfies mask-type (inequality) constraints. The method is based on an integral equation formulation, with local impedance boundary condition (IBC) approximation. The procedure yields the spatial distribution of the impedance, yet the process involves the synthesis of the equivalent current only. This current is constrained to correspond to a realizable surface impedance, i.e., passive, lossless, and with reactance values bounded by practical realizability limits. The current-based design avoids any solution of the forward problem, and the impedance is obtained from the synthesized current only at the end of the process. The procedure is gradient-based, with the gradient expressed in closed form. This allows handling large metasurfaces, with full spatial variability of the impedance in two dimensions. The method requires no a priori information, and all relevant operations in the iterative process can be evaluated with $O(N \log N)$ complexity. Application examples concentrate on the case of on-surface excitation and far-field pattern specifications; they show designs of circular and rectangular metasurface antennas of 20 wavelengths in size, with pencil- and shaped-beam patterns, and for both circular and linear polarization.**

***Index Terms*—Metasurfaces, antennas, integral equations, method of moments, impedance boundary condition, optimization.**

I. INTRODUCTION

FIELD manipulation via metasurfaces is a topic of continuously expanding relevance. Example of applications include low-profile antennas, (meta)lenses, polarizers, and (meta)radomes; reflectarrays and transmitarrays have also seen realization with metasurfaces. A recent addition to the list are reconfigurable intelligent surfaces (RIS) [1] proposed for 5G and beyond-5G environments. In all these applications, the metasurface interacts with an incident, assigned field and the interaction generates the radiated field; the metasurface is engineered so that the radiated field has the desired properties. Metasurfaces can be realized with a variety of technologies: currently, the most popular one is the use of printed conductive elements (e.g., patches, holes in a metalization, meanders) and all-metal pillars. Within printed-type structures, the main difference between the various classes is in terms of the number of metasurface layers: low-profile antennas are usually single-layer, while trasmit-type structures require more than one layer to ensure functionality and absence of reflection. Another difference is in the nature of the incident (forcing) field: in low-profile antennas it is generated by a feed embedded in the surface (e.g., through a vertical pin), which launches a guided surface wave in the grounded dielectric; in practically all other cases the feed is external and illuminates the metasurface.

The conception and systematic design of spatially varying metasurfaces has been initially based on wave physics and analytical considerations, e.g., [2]–[5]. These analytically-based approaches have made metasurface antennas a reality, but of course they cannot accommodate for arbitrary design specifications; this has prompted research into automated design algorithms, the category to which the present work belongs. Ideally, the process would be totally automatic, starting from specification and ending with the metasurface layout, requiring no extra information, assumptions, or user intervention.

In the current literature, the full design task is conveniently split into two subsequent phases via the (approximate) representation of the metasurface in terms of an *impedance boundary condition*. That is, the design aims at finding the spatial distribution of a surface impedance; after that, the final layout is achieved by finding the geometrical parameters of the considered unit cell so that it produces the previously determined impedance profile. This two-phase approach is the one followed by virtually all published works; it is interesting to note its robustness: in [6] it has been shown to be effective even for a non-flat structure (a conical horn). The present work deals with finding the spatial distribution of the metasurface surface impedance; the realization of the unit cells is not part of this work and can be done with a variety of existing approaches, e.g., [4], [7].

A. State of the Art of Automated Metasurface Design

In the following, we will label "2D" the cases in which one spatial coordinate is considered invariant or periodic in the design—thus ignorable—and "3D" when that restriction

---

Manuscript received April 19, 2005; revised August 26, 2015. This work was supported by the Italian Ministry of Research PRIN 2017S29ZLA "Metasurface Antennas for Space Applications". *(Corresponding author: Marcello Zucchi)*.

M. Zucchi and G. Vecchi are with the Department of Electronics and Telecommunications, Politecnico di Torino, Turin 10129, Italy (e-mail: marcello.zucchi@polito.it; giuseppe.vecchi@polito.it).

F. Vernì was with Politecnico di Torino at the time of performing this work; he is now with Huawei Milan Research Center, Huawei Technologies, Milan, Italy (e-mail: francesco.verni@huawei.com).

M. Righero is with the Advanced Computing, Photonics & Electromagnetics (CPE) area, Fondazione LINKS, Turin 10138, Italy (e-mail: marco.righero@linksfoundation.com).

This article has been accepted for publication in IEEE Transactions on Antennas and Propagation. This is the author's version which has not been fully edited and content may change prior to final publication. Citation information: DOI 10.1109/TAP.2023.3270715

is not present. We will also distinguish between two different types of field specifications: pattern-matching and mask-type inequalities. In pattern-matching, the objective is to obtain a given field by minimizing the distance from it. Mask-type specifications are more general (and more used in practice): an "ideal" pattern is not known in advance, instead the field amplitude is required to satisfy inequalities, i.e., to lie within upper and lower bounds; the spatial variations of these bounds are called "masks". A practically relevant sub-class of this problem is that in which one seeks to maximize the main beam gain (in a prescribed direction, e.g., broadside).

Consistent with the scope of this work, we will review only approaches aiming at the fully numerical design of the metasurface; for the same reason, we will not review the large body of literature on the design of unit cells.

2D methods: The approach in [8] employs a dual optimization considering equivalent currents and impedance at the same time, with an alternating type of optimization; this requires to solve the forward problem at each step. A method based on optimizing the currents only would dispense from the solution of the forward problem during the iterations: an important step in this direction is in [9] where losslessness is enforced directly; the resulting (non-convex) optimization instance was approached with a global optimization. This approach was further progressed in [10], employing a better scaling gradient-based optimization. As in the previous works, [11] considers explicitly a transmission-reflection problem through the (stacked) metasurface layers, i.e., for an exciting field not generated on-surface. For this problem, fields are represented in terms of traveling waves in each (sub-wavelength) unit cell: this allows to formulate the problem directly in terms of circuit parameters, with the currents expressed through them; as a result, the circuit elements are the direct unknowns of the inverse problem, with passivity and absence of losses automatically enforced. These important latter works address the problem of (phaseless) pattern matching—as opposed to mask-type (inequality) field specifications. A scattering approach to synthesis is also presented in [12]. In [13] a multi-layer, dual-band method is introduced for the design of reflective-type metasurfaces with pattern-matching requirements; the method builds upon the previous work in [14]. The design is done in two steps: initially, equivalent currents are synthesized without passivity requirements, and complex impedance values are obtained from these. In a second step, reactance values are optimized to match the field produced by the complex impedance. Finally, [15] addresses the electromagnetically consistent design of the surface impedance in RIS at a system level.

3D methods: The work in [16], [17] appears the first to employ equivalent currents solely, with the related numerical advantage, and it allows design of both scalar and tensor impedance. It formulates the problem as a field matching in amplitude and phase, with the scaling of the radiated field with respect to the incident one provided externally; increasingly sophisticated estimates of this ratio have been developed [18], [19]. In [20] equivalent currents are first found from radiated field mask-type requirements (on the footprint); a 3D realizable metasurface layout is subsequently obtained via optimization (also involving machine learning) and exploiting the degrees of freedom of non-radiating currents (similar to [21]). The work in [22] is in between 2D and 3D; it performs the automated design of a 2D metamaterial (variable in (x, y)) with a cylindrical symmetry (TE along z) using a 2D FEM forward problem with a constrained gradient-based method. A similar approach is adopted in [23], where the forward problem is dealt with in terms of a 2D circuit network solver using reduced-order models of the metastructure's unit cells to reduce the computational load. Finally, the works in [24] and [25] employ a global optimization, made possible by a drastic reduction of the number of degrees of freedom of the surface, via a physics-based parameterization deriving from previous analytical works. At each iteration, a solution to the forward problem is required; to reduce its cost, [24] exploits BOR symmetry, while [25] uses specialized entire-domain basis functions (introduced in [26]). Finally, global optimization of unit cells and the design of limited size binary metasurface apertures have also been reported [27].

B. Innovation

We present an automatic 3D method to design a metasurface of practically relevant size, without any restriction on the 2D spatial variation of the impedance profile, allowing arbitrary mask-type (inequalities) specifications on the radiated field, and including constraints on the values of the surface reactance—so as to ensure practical technological realizability.

This goal is reached with a method that involves the optimization of *only* the metasurface equivalent current, and a formulation of the optimization instance that employs piecewise-polynomial expressions of the current coefficients. To the best of the authors' knowledge, it is the first time this is presented.

The numerical challenges involved in the 3D problem, due to the size of the structure, are addressed by a formulation that is computationally efficient, in that all functional and gradient evaluations require only a limited number of matrix-vector products. A further manipulation allows to compute the cost functional and its gradient with almost-linear complexity via the so-called fast formulation of the forward problem. The proposed approach, however, is applicable even when fast methods are not available.

The incident field is arbitrary; special attention is given here to the case of on-surface excitation, as necessary in low-profile metasurface antennas. In this case, the scattering representation of [11] would be more difficult to apply, due to the interplay between a guided wave and the metasurface, with the wave traversing multiple unit cells.

At a difference with literature on current-only design [16], [17], field objectives, passivity and losslessness are obtained without any a priori information on the ratio between incident and radiated power, rendering the estimation of this ratio unnecessary. Radiated power in the angular region of interest is maximized *for a given incident power*: this minimizes reflection from the metasurface as well as the amplitude of the residual surface wave guided in the dielectric. Furthermore, this method does not rely on a separation between radiative and evanescent parts of the current spectrum.

This article has been accepted for publication in IEEE Transactions on Antennas and Propagation. This is the author's version which has not been fully edited and content may change prior to final publication. Citation information: DOI 10.1109/TAP.2023.3270715

Finally, recent approaches to enforce passivity have employed surface-wave constructs and non-local schemes (e.g., [28]–[30]). These appear to be inherently part of the automatic process proposed here, which operates on the surface globally.

II. BACKGROUND: FORWARD PROBLEM FORMULATION AND NUMERICAL CONSIDERATIONS

The metasurface is modelled as a layer of *Impedance Boundary Condition* (IBC) [31], which relates the tangential electric field to the jump of the tangential magnetic field:

$$\boldsymbol{E}_{\tan} = \overline{\overline{\boldsymbol{Z}}} \cdot \left[\hat{\boldsymbol{n}} \times (\boldsymbol{H}^{+} - \boldsymbol{H}^{-})\right] \tag{1}$$

for each point on $\mathcal{S}_{\mathrm{IBC}}$, where the space-dependent value of the impedance, $\overline{\overline{\boldsymbol{Z}}}$, is in general of tensorial nature. See Fig. 1 for a pictorial representation of a metasurface antenna.

In this work, we will restrict our attention to the case of a *scalar impedance* boundary condition, i.e., $\overline{\overline{\boldsymbol{Z}}} = Z\,\overline{\overline{\boldsymbol{I}}}$ (where $\overline{\overline{\boldsymbol{I}}}$ is the identity tensor). The method to be presented in the following sections is not restricted to the scalar case and can be adapted to tensor impedance, but a) there are theoretical issues to be discussed preliminarily, and b) this would obscure the nature of this presentation; hence, it will be postponed to a future communication.

By introducing the equivalent current density,

$$\boldsymbol{J} = \hat{\boldsymbol{n}} \times (\boldsymbol{H}^{+} - \boldsymbol{H}^{-}), \tag{2}$$

the electromagnetic problem is formulated as an *Electric Field Integral Equation* (EFIE-IBC):

$$\left[\boldsymbol{E}_{\mathrm{inc}}(\boldsymbol{r}) + \mathcal{L}\boldsymbol{J}(\boldsymbol{r})\right]_{\tan} = Z(\boldsymbol{r})\boldsymbol{J}(\boldsymbol{r}) \qquad \forall \boldsymbol{r} \in \mathcal{S}_{\mathrm{IBC}} \tag{3}$$

where $\boldsymbol{E}_{\mathrm{inc}}$ is the incident field radiated by the source in absence of the metasurface, and $\mathcal{L}$ is the *Electric Field Integral Operator* (EFIO) defined as

$$\mathcal{L}\boldsymbol{J}(\boldsymbol{r}) = \iint\limits_{\mathcal{S}_{\mathrm{IBC}}} \overline{\overline{\boldsymbol{G}}}^{\mathrm{EJ}}(\boldsymbol{r}, \boldsymbol{r}') \cdot \boldsymbol{J}(\boldsymbol{r}') \,\mathrm{d}S(\boldsymbol{r}'), \tag{4}$$

where $\overline{\overline{\boldsymbol{G}}}^{\mathrm{EJ}}$ is the multilayer dyadic Green's function for the (grounded or ungrounded) substrate [32]. It is noted that here the problem is formulated in terms of a transparent (two-sided) IBC, which requires the Green's function of the layered background medium. This approach has been shown to be significantly more stable than the one involving the opaque (one-sided) version of the IBC, which would do without the more complex mentioned Green's function [33]. It also allows for a better description of spatial dispersion (the effect of the dielectric substrate is fully described), and eases the passage from the impedance profile $Z(\boldsymbol{r})$ to the design of the individual unit cells (note that this step is not part of the present contribution).

For the numerical discretization we adopt the usual Method of Moments approach: we consider a mesh given by a tessellation of the surface $\mathcal{S}_{\mathrm{IBC}}$ composed of N_c triangular patches $\mathcal{S}_i$ and we approximate the sought current $\boldsymbol{J}(\boldsymbol{r})$ as a linear combination of Rao-Wilton-Glisson (RWG) basis functions $\boldsymbol{\Lambda}_n$ [34] defined on the N internal mesh edges,

$$\boldsymbol{J}(\boldsymbol{r}) = \sum_{n=1}^{N} I_n \,\boldsymbol{\Lambda}_n(\boldsymbol{r}). \tag{5}$$

We then test the integral equation (3) with the same set of functions (Galerkin's method) through the bilinear form

$$\langle\, \boldsymbol{a} \,, \boldsymbol{b} \,\rangle = \iint\limits_{\mathcal{S}_{\mathrm{IBC}}} \boldsymbol{a} \cdot \boldsymbol{b} \,\mathrm{d}S. \tag{6}$$

The problem reduces to the linear system

$$\mathsf{V}_{\mathrm{inc}} + \mathsf{L}\mathsf{I} = \mathsf{Z}\mathsf{I}, \tag{7}$$

where the array I collects the RWG basis coefficients I_n and the remaining quantities are defined as

$$(\mathsf{L})_{mn} = \langle\, \boldsymbol{\Lambda}_m \,, \mathcal{L}\boldsymbol{\Lambda}_n \,\rangle, \tag{8}$$

$$(\mathsf{Z})_{mn} = \langle\, \boldsymbol{\Lambda}_m \,, Z\boldsymbol{\Lambda}_n \,\rangle, \tag{9}$$

$$(\mathsf{V}_{\mathrm{inc}})_m = \langle\, \boldsymbol{\Lambda}_m \,, \boldsymbol{E}_{\mathrm{inc}} \,\rangle \tag{10}$$

If radiated field specifications are given at arbitrary points, radiation is obtained via application of the EFIO, $\mathcal{L}\boldsymbol{J}$. Instead, when field specifications are defined in the far-field (FF) region, the corresponding *radiation operator* $\mathcal{R}$ is given by

$$\mathcal{R}\boldsymbol{J}(\hat{\boldsymbol{r}}) = \frac{\mathrm{j}k_0}{2\pi} \,\overline{\overline{\boldsymbol{G}}}^{\mathrm{FF}}(\hat{\boldsymbol{r}}) \cdot \iint\limits_{\mathcal{S}_{\mathrm{IBC}}} \boldsymbol{J}(\boldsymbol{r}') \,\mathrm{e}^{\mathrm{j}k_0 \hat{\boldsymbol{r}} \cdot \boldsymbol{r}'} \,\mathrm{d}S(\boldsymbol{r}') \tag{11}$$

where the multilayer FF tensor is defined as

$$\overline{\overline{\boldsymbol{G}}}^{\mathrm{FF}}(\hat{\boldsymbol{r}}) = -g^{\mathrm{TM}}(\hat{\boldsymbol{r}}) \,\hat{\boldsymbol{\theta}}\hat{\boldsymbol{\rho}} - \cos\theta \, g^{\mathrm{TE}}(\hat{\boldsymbol{r}}) \,\hat{\boldsymbol{\varphi}}\hat{\boldsymbol{\varphi}}. \tag{12}$$

Here, g^{TM} and g^{TE} are the longitudinal transmission line transfer functions for the TE and TM components [35, p. 1182], while θ and ϕ are the polar and azimuthal angles describing the direction of radiation. The unit vectors $\hat{\boldsymbol{r}}$, $\hat{\boldsymbol{\theta}}$ and $\hat{\boldsymbol{\varphi}}$ are those of the spherical coordinate system, and

$$\hat{\boldsymbol{\rho}} = \cos\phi \,\hat{\boldsymbol{x}} + \sin\phi \,\hat{\boldsymbol{y}}. \tag{13}$$

We use the shorthand $\boldsymbol{E}(\hat{\boldsymbol{r}}, \mathsf{I})$ to indicate the field obtained when (11) is applied to a current expressed in the form (5), to emphasize the dependency on the coefficients collected in I.

Enforcement of radiated field specifications involves sampling the field at a discrete set of points; for the case of far-field specifications, the sampling points $\hat{\boldsymbol{r}}_j$ lie on the unit sphere, and are identified by the spherical coordinates (θ_j, ϕ_j). For each sampling point, two orthogonal polarizations tangential to the sphere are defined along $\hat{\boldsymbol{\theta}}$ and $\hat{\boldsymbol{\varphi}}$. The radiated field samples at $\hat{\boldsymbol{r}}_j, j = 1, \ldots, N_{\mathrm{f}}$ are assembled in column vectors $\mathsf{E}_\theta, \mathsf{E}_\varphi \in \mathbb{C}^{N_{\mathrm{f}}}$ and, considering the discretization of the current (5), they may be expressed as:

$$\mathsf{E}_\theta = \mathsf{E}_\theta^0 + \mathbf{R}_\theta \mathsf{I}, \tag{14}$$

$$\mathsf{E}_\varphi = \mathsf{E}_\varphi^0 + \mathbf{R}_\varphi \mathsf{I}, \tag{15}$$

where the fields E_θ^0 and E_φ^0 are those due to the incident field (present in the absence of the metasurface), and the radiation matrices $\mathbf{R}_\theta, \mathbf{R}_\varphi \in \mathbb{C}^{N_{\mathrm{f}} \times N}$ are defined as follows:

$$(\mathbf{R}_\theta)_{jn} = \hat{\boldsymbol{\theta}}_j \cdot \mathcal{R}\boldsymbol{\Lambda}_n(\hat{\boldsymbol{r}}_j), \tag{16}$$

$$(\mathbf{R}_\varphi)_{jn} = \hat{\boldsymbol{\varphi}}_j \cdot \mathcal{R}\boldsymbol{\Lambda}_n(\hat{\boldsymbol{r}}_j). \tag{17}$$

We note that, in the above, the radiated far-field has been normalized to $\exp(-\mathrm{j}k_0 r)/r$.

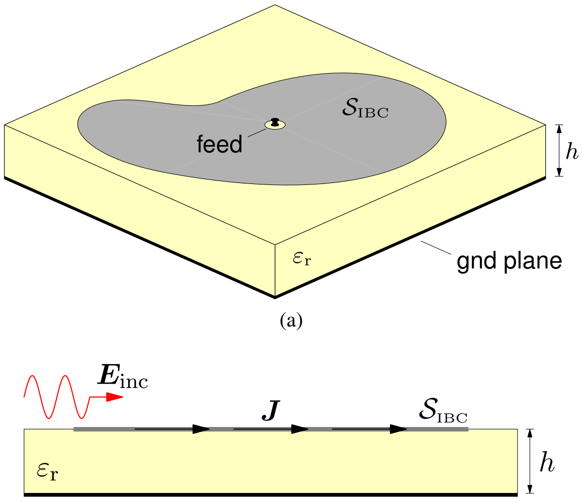

(a)

(b)

Fig. 1. Geometry of the metasurface antenna: (a) 3D view, for the case in which the source of the incident field is on-surface, (b) cross section with the equivalent currents $\boldsymbol{J}$.

In the design of electrically large antennas, it is necessary to exploit fast numerical algorithms for feasibility reasons; the optimization strategy must take this into account, as will be detailed later. Fast factorizations (e.g., [36]) are related to iterative solutions of the forward problem (7); they allow to store only near-field interactions of the EFIO matrix L (with $O(N)$ storage requirement) and to perform matrix-vector products LI with $O(N \log N)$ complexity (i.e., with $O(N \log N)$ operations per product). Fast factorizations are also required to accelerate matrix-vector products in the computation of the radiated fields (14)–(15), and to avoid the computation and storage of the radiation matrices (16)–(17).

In this work, the matrix-vector products involving the EFIO operator are performed by means of a GIFFT algorithm [37], [38], while far-field radiation is computed by an upward pass of the multilevel fast multipole algorithm (MLFMA) with FFT interpolation on a regular grid of far-field points in the u-v space [36, Sec. 3.5.5].

III. PROBLEM STATEMENT

The design of metasurface antennas starts with the definition of the surface geometry and of the source, the latter resulting in the specification of the incident field. The aim is to obtain an impedance profile that is physically and technologically realizable, and that radiates a field pattern obeying the specifications when it interacts with the source field.

a) Realizability: To obtain a physically realizable impedance we need to impose specific constraints: the metasurface must be locally *passive* and *lossless*, meaning that for each point on the surface, the active power should neither be dissipated, nor provided, i.e.,

$$\operatorname{Re} Z(\boldsymbol{r}) = 0, \quad \forall \boldsymbol{r} \in \mathcal{S}_{\text{IBC}}. \tag{18}$$

Moreover, the range of realizable reactance values depends on the chosen unit cell type, the employed technology and practical (e.g., size) limits; these bounds must be enforced in the design process,

$$X_{\text{L}} \leq \operatorname{Im} Z(\boldsymbol{r}) \leq X_{\text{U}}, \quad \forall \boldsymbol{r} \in \mathcal{S}_{\text{IBC}}. \tag{19}$$

These two requirements ensure that the metasurface can be implemented by means of the chosen unit cells.

b) Field specifications: The radiated field specifications may be both in the far-field region or closer; here we concentrate on far-field specifications, expressed in terms of the field amplitude (power density); we consider both the co- ("co") and cross-polarized ("cx") components, as well as the total ("tot") amplitude:

$$F^{\text{co}}(\hat{\boldsymbol{r}}, \mathsf{I}) = \left|\boldsymbol{E}(\hat{\boldsymbol{r}}, \mathsf{I}) \cdot \hat{\boldsymbol{p}}^{*}(\hat{\boldsymbol{r}})\right|^{2} \tag{20}$$

$$F^{\text{cx}}(\hat{\boldsymbol{r}}, \mathsf{I}) = \left|\boldsymbol{E}(\hat{\boldsymbol{r}}, \mathsf{I}) \cdot \hat{\boldsymbol{q}}^{*}(\hat{\boldsymbol{r}})\right|^{2} \tag{21}$$

$$F^{\text{tot}}(\hat{\boldsymbol{r}}, \mathsf{I}) = \left|\boldsymbol{E}(\hat{\boldsymbol{r}}, \mathsf{I})\right|^{2} \tag{22}$$

where $\hat{\boldsymbol{p}}$ and $\hat{\boldsymbol{q}} = \hat{\boldsymbol{r}} \times \hat{\boldsymbol{p}}^{*}$ are the co- and cross-polarization unit vectors, respectively.

Field specifications are of the *mask type*, i.e., defined via *inequalities* of the kind

$$M_{\text{L}}(\hat{\boldsymbol{r}}, \mathsf{I}) \leq F(\hat{\boldsymbol{r}}, \mathsf{I}) \leq M_{\text{U}}(\hat{\boldsymbol{r}}, \mathsf{I}) \tag{23}$$

for each considered far-field direction $\hat{\boldsymbol{r}}$. Mask values must typically be defined in terms of directivity or gain. We observe that pattern-matching, i.e., fitting a specific (amplitude) field pattern, is a special case of the above (with $M_{\text{L}} = M_{\text{U}}$), that is easier to address as it does not require inequalities.

Specification of an *absolute* lower bound to the main lobe (co-polarization) may be a requirement in some designs; on the other hand, sidelobe and cross-polarization levels have to be defined *relative* to the *actual* level in the main beam. In this way, the relative levels comply with the specifications even when the main lobe requirement is not met by the solution. This can be made specific as follows: let $\hat{\boldsymbol{r}}_0$ be the specified beam pointing direction; we introduce a reference main-lobe level as the average over a small angular region Ω_0 around the maximum radiation direction $\hat{\boldsymbol{r}}_0$,

$$F_{\text{ref}}(\mathsf{I}) = \frac{1}{\Omega_0} \iint\limits_{\Omega_0} F^{\text{co}}(\hat{\boldsymbol{r}}, \mathsf{I}) \, \mathrm{d}\Omega(\hat{\boldsymbol{r}}). \tag{24}$$

The above is a generalization of the amplitude in the specified beam direction, $F^{\text{co}}(\hat{\boldsymbol{r}}_0)$, to which it reduces in a trivial manner; use of this averaged level typically makes the optimization instance more robust, especially in shaped-beam design instances (e.g., flat-top). Given a lower bound M_0 for the reference level, the only absolute requirement will thus be

$$F_{\text{ref}}(\mathsf{I}) \geq M_0, \tag{25}$$

with all others becoming relative to F_{ref}.

Regarding the relative specifications, it is convenient to divide them into those for the main lobe (ML) region Ω_{ML}, and those for the side-lobe (SL) region Ω_{SL}, as they are functionally different. Overall, this results in the following set of specifications:

$$M_{\text{L}}^{\text{co}}(\hat{\boldsymbol{r}}, \mathsf{I}) \leq F^{\text{co}}(\hat{\boldsymbol{r}}, \mathsf{I}) \leq M_{\text{U}}^{\text{co}}(\hat{\boldsymbol{r}}, \mathsf{I}), \quad \hat{\boldsymbol{r}} \in \Omega_{\text{ML}} \tag{26}$$

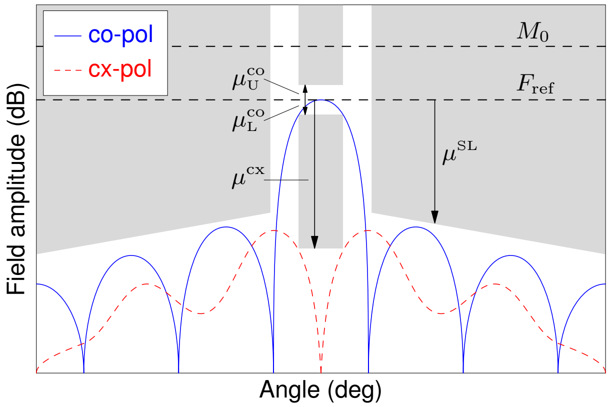

Fig. 2. Example of far-field specifications: objective level M_0, reference level F_{ref}, main lobe co-pol mask $M_{\mathrm{L}}^{\mathrm{co}}$, $M_{\mathrm{U}}^{\mathrm{co}}$, cross-pol mask $M_{\mathrm{U}}^{\mathrm{cx}}$ and side lobes mask $M_{\mathrm{U}}^{\mathrm{tot}}$. Vertical arrows indicate relative levels.

where

$$M_{\mathrm{U/L}}^{\mathrm{co}}(\hat{\boldsymbol{r}}, \mathsf{I}) = \mu_{\mathrm{U/L}}^{\mathrm{co}}(\hat{\boldsymbol{r}})\, F_{\mathrm{ref}}(\mathsf{I}) \tag{27}$$

with the upper requirement being absent in pencil-beam type specifications, and

$$F^{\mathrm{cx}}(\hat{\boldsymbol{r}}, \mathsf{I}) \leq M^{\mathrm{cx}}(\hat{\boldsymbol{r}}, \mathsf{I}), \quad \hat{\boldsymbol{r}} \in \Omega_{\mathrm{ML}} \tag{28}$$

$$F^{\mathrm{tot}}(\hat{\boldsymbol{r}}, \mathsf{I}) \leq M^{\mathrm{tot}}(\hat{\boldsymbol{r}}, \mathsf{I}), \quad \hat{\boldsymbol{r}} \in \Omega_{\mathrm{SL}} \tag{29}$$

where

$$M^{\mathrm{cx}}(\hat{\boldsymbol{r}}, \mathsf{I}) = \mu^{\mathrm{cx}}(\hat{\boldsymbol{r}})\, F_{\mathrm{ref}}(\mathsf{I}) \tag{30}$$

$$M^{\mathrm{tot}}(\hat{\boldsymbol{r}}, \mathsf{I}) = \mu^{\mathrm{SL}}(\hat{\boldsymbol{r}})\, F_{\mathrm{ref}}(\mathsf{I}) \tag{31}$$

All these requirements are summarized graphically in Fig. 2.

IV. CURRENT-BASED DESIGN

A. *Strategy*

The outcome of the design must be the spatial distribution of the surface impedance; however, we formulate the problem in such a way that it involves *only* the equivalent current—not the impedance. On exit, the process yields the "right" current, from which a corresponding impedance is obtained. The complete procedure is detailed in Alg. 1.

This current-based design process avoids the solution of the forward problem (7) at each step, with obvious advantages in terms of numerical complexity. Of course, this is possible only if the current being sought-for can be constrained to correspond to a passive and lossless surface, in addition to radiating a field that satisfies the related requirements. Moreover, we want the reactance associated to the current to be bounded by practical realizability limits—again, without computing this reactance explicitly during the process.

We formulate the design as an *unconstrained* optimization problem, where the fitness is expressed in terms of cost functionals to be minimized. The synthesized current is the solution of the following problem:

$$\mathsf{I}^{\star} = \underset{\mathsf{I} \in \mathbb{C}^N}{\arg\min}\, f(\mathsf{I}) \tag{32}$$

where the overall functional f is the sum of a term f_{rlz} that expresses the compliance with realizability constraints, and of a term f_{rad} that quantifies the fitness of the radiated field,

$$f(\mathsf{I}) = f_{\mathrm{rlz}}(\mathsf{I}) + f_{\mathrm{rad}}(\mathsf{I}) \tag{33}$$

Algorithm 1 Algorithm for the design of the surface impedance profile $Z(\boldsymbol{r})$.

```
Input: $\mathsf{I}_0, X_{\mathrm{L}}, X_{\mathrm{U}}, \Omega_0, \Omega_{\mathrm{ML}}, \Omega_{\mathrm{SL}}, M_0, \mu_{\mathrm{L}}^{\mathrm{co}}, \mu_{\mathrm{U}}^{\mathrm{co}}, \mu^{\mathrm{cx}}, \mu^{\mathrm{tot}}$
Output: $\mathsf{z}$
  $\mathsf{I} \leftarrow \mathsf{I}_0$
  $k \leftarrow 0$
  while $k \leq K^{\max}$ do
      Compute $P$, $Q$, $\mathcal{J}$, $\mathcal{E}$                                   ▷ (49)–(52)
      Compute $\rho^{\mathrm{act}}$, $\rho^{\mathrm{rct}}$, $\rho^{\mathrm{scal}}$        ▷ (46)–(48)
      Compute $f_{\mathrm{rlz}}$                                                        ▷ (45)

      Compute $F_{\mathrm{ref}}$, $F^{\mathrm{co}}$, $F^{\mathrm{cx}}$, $F^{\mathrm{tot}}$      ▷ (60), (70)–(72)
      Compute $M_{\mathrm{L}}^{\mathrm{co}}$, $M_{\mathrm{U}}^{\mathrm{co}}$, $M^{\mathrm{cx}}$, $M^{\mathrm{tot}}$   ▷ (63)–(65)
      Compute $\rho_{\mathrm{ref}}$, $\rho^{\mathrm{co}}$, $\rho^{\mathrm{cx}}$, $\rho^{\mathrm{tot}}$  ▷ (62), (67)–(69)
      Compute $f_{\mathrm{rad}}$                                                        ▷ (66)

      $f \leftarrow f_{\mathrm{rlz}} + f_{\mathrm{rad}}$

      Compute $\tilde{\nabla}\rho^{\mathrm{act}}$, $\tilde{\nabla}\rho^{\mathrm{rct}}$, $\tilde{\nabla}\rho^{\mathrm{scal}}$   ▷ (74)–(77), (80), (82)
      Compute $\tilde{\nabla} f_{\mathrm{rlz}}$

      Compute $\tilde{\nabla}\rho_{\mathrm{ref}}$, $\tilde{\nabla}\rho^{\mathrm{co}}$, $\tilde{\nabla}\rho^{\mathrm{cx}}$, $\tilde{\nabla}\rho^{\mathrm{tot}}$   ▷ (83)–(85), (87)
      Compute $\tilde{\nabla} f_{\mathrm{rad}}$

      $\tilde{\nabla} f \leftarrow \tilde{\nabla} f_{\mathrm{rlz}} + \tilde{\nabla} f_{\mathrm{rad}}$

      Set $\beta_k$                                                                     ▷ (90)
      Set $\mathsf{p}_k$                                                                ▷ (89)
      Compute $\alpha_k$                                                                ▷ (91)
      $\mathsf{I}_{k+1} \leftarrow \mathsf{I}_k + \alpha_k \mathsf{p}_k$
      $k \leftarrow k + 1$
  end while
  Compute $\mathsf{z}$                                                                  ▷ (103), (105)
```

As explained above, it is crucial to express these terms as functions of the current *only*; this point will be addressed in Secs. IV-B and IV-C.

An important observation is that requirements involving inequalities, like those of field masks in (23) or reactance bounds (19), are conveniently expressed as quantities to be minimized by means of the ramp function

$$\mathrm{r}(x) = \max(x, 0) \tag{34}$$

with which a condition of the type $a \leq b$ becomes $\mathrm{r}(a-b) = 0$.

For the class of constraints of relevance here, the associated minimization instance is non-convex. Hence, strategies to overcome the non-convexity shortcomings, and in particular local trappings, are very important. Inspired by [9], our choice is to resort to functionals that are of polynomial type in the current coefficients, in particular fourth-degree polynomials, with added rectification (via the ramp function) where needed.

The most general expression for the functional takes the form

$$\begin{aligned} f(\mathsf{I}) &= \sum_{d=1}^{N_d} q_d(\mathsf{I})\, s_d(\mathsf{I}) + \sum_{e=1}^{N_e} \mathrm{r}^2(t_e(\mathsf{I})) \\ &= \mathsf{q}^{\mathsf{T}}\mathsf{s} + \mathrm{r}\,(\mathsf{t})^{\mathsf{T}}\,\mathrm{r}\,(\mathsf{t}) \end{aligned} \tag{35}$$

where $\mathrm{r}^2(x) = \max(x,0)^2$ is a C^1 function (continuous with continuous derivative); N_d and N_e are the total number of terms in the two functionals. We have defined the arrays

$$\mathsf{q} = [q_1(\mathsf{I}), \ldots, q_d(\mathsf{I}), \ldots, q_{N_d}(\mathsf{I})]^{\mathsf{T}} \tag{36}$$

$$\mathsf{s} = [s_1(\mathsf{I}), \ldots, s_d(\mathsf{I}), \ldots, s_{N_d}(\mathsf{I})]^{\mathsf{T}} \tag{37}$$

$$\mathsf{t} = [t_1(\mathsf{I}), \ldots, t_e(\mathsf{I}), \ldots, t_{N_e}(\mathsf{I})]^{\mathsf{T}} \tag{38}$$

where q_d, s_d and t_e are multivariable quadratic functions of the current coefficients, i.e., of the form

$$q_d \text{ or } s_d \text{ or } t_d = \mathrm{Re}\left(\mathsf{I}^{\mathsf{H}}\mathbf{\mathsf{A}}_d\mathsf{I} + \mathsf{I}^{\mathsf{H}}\mathsf{b}_d + c_d\right) \tag{39}$$

where $\mathbf{\mathsf{A}}_d \in \mathbb{C}^{N\times N}$ are positive definite matrices, $\mathsf{b}_d \in \mathbb{C}^N$ are column vectors and $c_d \in \mathbb{C}$ are constants. The advantage of this choice is apparent: for even-degree polynomials, the functional is bounded below, and goes to $+\infty$ as $\|\mathsf{I}\| \longrightarrow +\infty$. Moreover, a polynomial of degree four limits the number of possible local minima, while still allowing enough flexibility in the definition of the functional. Finally, the problem is formulated so that the matrices $\mathbf{\mathsf{A}}_d$ are such that the computation of each term of (35) can be accelerated to quasi-linear complexity (either $\mathbf{\mathsf{A}}_d$ is sparse or the matrix-vector product $\mathbf{\mathsf{A}}_d\mathsf{I}$ can be computed with fast algorithms).

For the minimization of (32) we employ a *non-linear conjugate gradient* algorithm [39, p. 121]. Given the large size of the problem, the numerical cost of computing the functional and its gradient at each iteration is an issue of paramount importance; as will be seen in Sec. IV-D, this impacts on the way the gradient is expressed. In particular, all operations involved in the computation of the near- or far-field radiated by a given current can be performed with the fast factorizations mentioned in Sec. II, with $O(N)$ memory requirements and $O(N \log N)$ complexity. Hence, all operations in the computation of the functional and of its gradient will be cast in such a way to be expressible in this form.

The other relevant step is the line search that must be carried out at each step of the iterative process. This is a deceivingly simple task, as it involves only a one-dimensional minimization along the search direction, which in principle can be performed with a variety of standard approaches. However, as is well known in the literature, the difficult part is finding the *interval* in which this search must be carried out. Our polynomial approach will allow to perform this in an analytical (possibly iterative), definite manner.

Finally, we have chosen not to enforce any smoothing of the current in the optimization; this could be done in different ways (see, e.g., [11]), but our choice avoids additional parameters to set, and will allow to check the intrinsic degree of regularity of the solution.

B. Enforcement of realizability constraints

As discussed, realizability requires local passivity and absence of losses, as well as bounds on the impedance values. Passivity and losslessness can be expressed directly in terms of the (local) active power density; moreover, we observe that the magnitude of the reactance can be linked to the (local) reactive power density. Hence, all realizability constraints can be cast in terms of power densities. This allows to express them in terms of the current only, in such a way that they also satisfy our requirement of being of polynomial nature.

We therefore start from the basic power density across a surface (see App. A),

$$\tilde{p}(\boldsymbol{r}) = \boldsymbol{E}\cdot\boldsymbol{J}^* = P + \mathrm{j}Q \tag{40}$$

that is related to the local impedance via the IBC as

$$\tilde{p}(\boldsymbol{r}) = Z\,|\boldsymbol{J}|^2 = \mathrm{Re}\,Z\,|\boldsymbol{J}|^2 + \mathrm{j}\,\mathrm{Im}\,Z\,|\boldsymbol{J}|^2\,. \tag{41}$$

The requirement for passivity and losslessness imposes that $P = 0$, i.e.,

$$\mathrm{Re}\left(\boldsymbol{E}\cdot\boldsymbol{J}^*\right) = 0. \tag{42}$$

In order to preserve passivity, one needs to enforce this condition locally in an explicit manner [9] (otherwise, one could have zero global dissipated power, but with active terms with $P < 0$ compensating losses).

The requirement (19) are related to the reactive power density via (41), resulting in

$$X_{\mathrm{L}}\,|\boldsymbol{J}|^2 \le \mathrm{Im}\left(\boldsymbol{E}\cdot\boldsymbol{J}^*\right) \le X_{\mathrm{U}}\,|\boldsymbol{J}|^2\,. \tag{43}$$

Finally, we note that, as the impedance does not appear in the conditions above, there is no guarantee that the obtained current is such as to correspond to a scalar impedance; hence, here we will enforce the scalarity condition explicitly. A necessary condition for the impedance to be scalar is that:

$$|\boldsymbol{E}\cdot\boldsymbol{J}^*| = |\boldsymbol{E}|\,|\boldsymbol{J}| \tag{44}$$

All the above conditions must hold locally everywhere; in accordance with our cell-based spatial discretization scheme, we will enforce these conditions in the average sense over each cell.

We recall here the important observation that inequality conditions like (43) can be expressed in terms of the ramp function; however, this function does not have a continuous derivative. For this reason, we employ the *squared ramp function*, $\mathrm{r}^2(x) = \max(x,0)^2$, which is a continuous function with continuous derivative. This allows the use of inequalities in the functional definition at the only expense of having *piecewise* polynomial functions, but everywhere continuous and differentiable.

With the above stipulations, the conditions of passivity and losslessness (“act”), of the reactance bounds (“rct”), and of scalarity (“scal”) result in a cost function that is the sum of three contribution:

$$f_{\mathrm{rlz}} = w_{\mathrm{act}}\sum_{i=1}^{N_{\mathrm{c}}}\rho_i^{\mathrm{act}} + w_{\mathrm{rct}}\sum_{i=1}^{N_{\mathrm{c}}}\rho_i^{\mathrm{rct}} + w_{\mathrm{scal}}\sum_{i=1}^{N_{\mathrm{c}}}\rho_i^{\mathrm{scal}} \tag{45}$$

The weights w_{act}, w_{rct} and w_{scal} have to be assigned a priori, like in all optimization problems of multi-objective nature. The cell-wise terms are defined as follows:

$$\rho_i^{\mathrm{act}} = {P_i}^2 \tag{46}$$

$$\rho_i^{\mathrm{rct}} = \mathrm{r}^2(X_{\mathrm{L}}\mathcal{J}_i - Q_i) + \mathrm{r}^2(Q_i - X_{\mathrm{U}}\mathcal{J}_i) \tag{47}$$

$$\rho_i^{\mathrm{scal}} = \mathcal{E}_i\,\mathcal{J}_i - \left({P_i}^2 + {Q_i}^2\right) \tag{48}$$

where

$$\begin{aligned} P_i &= \mathrm{Re}\iint_{\mathcal{S}_i} \boldsymbol{E}\cdot\boldsymbol{J}^*\,\mathrm{d}S = \mathrm{Re}\,(\mathsf{I}^{\mathsf{H}}\mathbf{\Gamma}_i\mathsf{V}) \\ &= \mathrm{Re}\left(\mathsf{I}^{\mathsf{H}}(\mathbf{\Gamma}_i\mathbf{K})\mathsf{I} + \mathsf{I}^{\mathsf{H}}(\mathbf{\Gamma}_i\mathsf{V}'_{\mathrm{inc}})\right) \end{aligned} \tag{49}$$

$$\begin{aligned} Q_i &= \mathrm{Im}\iint_{\mathcal{S}_i} \boldsymbol{E}\cdot\boldsymbol{J}^*\,\mathrm{d}S = \mathrm{Im}\,(\mathsf{I}^{\mathsf{H}}\mathbf{\Gamma}_i\mathsf{V}) \\ &= \mathrm{Im}\left(\mathsf{I}^{\mathsf{H}}(\mathbf{\Gamma}_i\mathbf{K})\mathsf{I} + \mathsf{I}^{\mathsf{H}}(\mathbf{\Gamma}_i\mathsf{V}'_{\mathrm{inc}})\right) \end{aligned} \tag{50}$$

$$\mathcal{J}_i = \iint_{\mathcal{S}_i} |\boldsymbol{J}|^2\,\mathrm{d}S = \mathsf{I}^{\mathsf{H}}\mathbf{\Gamma}_i\mathsf{I} \tag{51}$$

$$\begin{aligned} \mathcal{E}_i = \iint_{\mathcal{S}_i} |\boldsymbol{E}|^2\,\mathrm{d}S &= \mathsf{V}^{\mathsf{H}}\mathbf{\Gamma}_i\mathsf{V} = \mathsf{I}^{\mathsf{H}}(\mathbf{K}^{\mathsf{H}}\mathbf{\Gamma}_i\mathbf{K})\mathsf{I} \\ &+ 2\,\mathrm{Re}\left(\mathsf{I}^{\mathsf{H}}(\mathbf{K}^{\mathsf{H}}\mathbf{\Gamma}_i\mathsf{V}'_{\mathrm{inc}})\right) + \mathsf{V}'^{\mathsf{H}}_{\mathrm{inc}}\mathbf{\Gamma}_i\mathsf{V}'_{\mathrm{inc}}. \end{aligned} \tag{52}$$

For convenience, we have introduced the following quantities:

$$\mathsf{V} = \mathbf{G}^{-1}(\mathsf{V}_{\mathrm{inc}} + \mathbf{L}\mathsf{I}) = \mathsf{V}'_{\mathrm{inc}} + \mathbf{K}\mathsf{I} \tag{53}$$

$$\mathbf{K} = \mathbf{G}^{-1}\mathbf{L}, \quad \mathsf{V}'_{\mathrm{inc}} = \mathbf{G}^{-1}\mathsf{V}_{\mathrm{inc}}, \tag{54}$$

where $\mathbf{G} \in \mathbb{R}^{N\times N}$ is the Gram matrix of the RWG basis functions, defined as

$$(\mathbf{G})_{mn} = \iint\limits_{\mathcal{S}_{\mathrm{IBC}}} \boldsymbol{\Lambda}_m(\boldsymbol{r})\cdot\boldsymbol{\Lambda}_n(\boldsymbol{r})\,\mathrm{d}\boldsymbol{r} \tag{55}$$

and $\mathbf{\Gamma}_i \in \mathbb{R}^{N\times N}$ is the local Gram matrix for the i-th cell, defined as

$$(\mathbf{\Gamma}_i)_{mn} = \iint\limits_{\mathcal{S}_i} \boldsymbol{\Lambda}_m(\boldsymbol{r})\cdot\boldsymbol{\Lambda}_n(\boldsymbol{r})\,\mathrm{d}\boldsymbol{r}. \tag{56}$$

At most three RWG basis have their support on a single cell, therefore each matrix $\mathbf{\Gamma}_i$ is extremely sparse, with $O(1)$ non-zero entries.

C. Enforcement of field specifications

We solve for a current associated to a given incident field, and thus with a known source power; this allows to define bounds on the maximum achievable radiated power. In turns, this permits to transform the maximization of the radiated power into the minimization of the difference with respect to its theoretical maximum.

We indicate by P_{inc} the power associated to the (given) incident field $\boldsymbol{E}_{\mathrm{inc}}$; it is then natural and practically relevant to express the radiated field in terms of the *realized gain* [40],

$$G_{\mathrm{r}}(\hat{\boldsymbol{r}},\mathsf{I}) = \frac{|\boldsymbol{E}(\hat{\boldsymbol{r}},\mathsf{I})|^2/\eta_0}{P_{\mathrm{inc}}/4\pi} \tag{57}$$

where η_0 is the free-space impedance, and $\boldsymbol{E}(\hat{\boldsymbol{r}},\mathsf{I})$ is the far-field radiated by a given current, with the normalization of Sec. II. Hence, the specification mask in (23) will be given by

$$M(\hat{\boldsymbol{r}},\mathsf{I}) = \frac{\eta_0}{4\pi}P_{\mathrm{inc}}\,G_{\mathrm{r}}(\hat{\boldsymbol{r}},\mathsf{I}). \tag{58}$$

We observe that—neglecting losses—the difference between the incident power P_{inc} (associated to the incident field) and the radiated power P_{rad} is due the power trapped in the surface wave guided by the infinite dielectric. The latter is the sum of the power due to metasurface reflection P_{refl} and the (residual) power traveling outwards P_{out} that is diffracted by the antenna rim (diffraction is not accounted for in all methods employing an infinite dielectric),

$$P_{\mathrm{inc}} = P_{\mathrm{rad}} + P_{\mathrm{refl}} + P_{\mathrm{out}}. \tag{59}$$

As a result, maximizing the radiated power for a given incident power allows to directly account for possible anomalous reflection due to bandgap (typical in 1D leaky wave structures) in this automatic process; otherwise said, the present approach also optimizes the reflection of the incident field by the metasurface toward the source. In addition, it also minimizes the power of the outward traveling surface wave, and hence the effect of its rim diffraction.

Finally, in the above considerations—for the sake of clarity—we have referred to the total radiated power P_{rad} instead of the power radiated in the main beam $P_{\mathrm{rad},\Omega_0}$; since the unwanted power radiated outside the main beam is controlled by side-lobe minimization, there is no practical difference to the discussion above.

The radiated field requirements in (26), (28)–(29) are all expressed as inequalities; using the approach described above, they can be cast directly in terms of functionals to be minimized employing the sampling and the expression of the radiation operator described in Sec. III.

We begin with the reference level F_{ref} in (24), which is now made explicit as

$$F_{\mathrm{ref}}(\mathsf{I}) = \frac{1}{\Omega_0}\sum_{j\in\Omega_0} F_j^{\mathrm{co}}\Delta\Omega_j \approx \frac{1}{N_0}\sum_{j\in\Omega_0} F_j^{\mathrm{co}}, \tag{60}$$

where we use the shorthand $F_j^{\mathrm{co}} = F^{\mathrm{co}}(\hat{\boldsymbol{r}}_j,\mathsf{I})$. With reference to (25), the maximization of F_{ref} can be equivalently expressed as the minimization of its difference with respect to the desired lower bound M_0,

$$M_0 - F_{\mathrm{ref}}(\mathsf{I}) \le 0 \tag{61}$$

and the related functional is immediately found to be

$$\rho_{\mathrm{ref}} = \mathrm{r}^2\big(M_0 - F_{\mathrm{ref}}(\mathsf{I})\big). \tag{62}$$

With the above expressions, the mask bounding values result in

$$M^{\mathrm{co}}_{\mathrm{U/L},j}(\mathsf{I}) = \mu^{\mathrm{co}}_{\mathrm{U/L}}(\hat{\boldsymbol{r}}_j)\,F_{\mathrm{ref}}(\mathsf{I}), \tag{63}$$

$$M^{\mathrm{cx}}_j(\mathsf{I}) = \mu^{\mathrm{cx}}(\hat{\boldsymbol{r}}_j)\,F_{\mathrm{ref}}(\mathsf{I}), \tag{64}$$

$$M^{\mathrm{tot}}_j(\mathsf{I}) = \mu^{\mathrm{SL}}(\hat{\boldsymbol{r}}_j)\,F_{\mathrm{ref}}(\mathsf{I}) \tag{65}$$

With these, the inequality constraints result in the following functional:

$$f_{\mathrm{rad}} = \rho_{\mathrm{ref}} + w_{\mathrm{ML}} \sum_{j \in \mathrm{ML}} (\rho_j^{\mathrm{co}} + \rho_j^{\mathrm{cx}}) + w_{\mathrm{SL}} \sum_{j \in \mathrm{SL}} \rho_j^{\mathrm{tot}} \tag{66}$$

where

$$\rho_j^{\mathrm{co}} = \mathrm{r}^2(M_{\mathrm{L},j}^{\mathrm{co}} - F_j^{\mathrm{co}}) + \mathrm{r}^2(F_j^{\mathrm{co}} - M_{\mathrm{U},j}^{\mathrm{co}}) \tag{67}$$

$$\rho_j^{\mathrm{cx}} = \mathrm{r}^2(F_j^{\mathrm{cx}} - M_{\mathrm{U},j}^{\mathrm{cx}}) \tag{68}$$

$$\rho_j^{\mathrm{tot}} = \mathrm{r}^2(F_j^{\mathrm{tot}} - M_{\mathrm{U},j}^{\mathrm{tot}}) \tag{69}$$

with the shorthand notation $F_j^{\mathrm{cx/tot}} = F^{\mathrm{cx/tot}}(\hat{\boldsymbol{r}}_j, \mathsf{I})$. Field amplitudes are computed according to (20)–(22) and the employed discretization:

$$F_j^{\mathrm{co}} = \left|E_j^{\mathrm{co}}\right|^2, \qquad E_j^{\mathrm{co}} = E_j^{\theta}\, \hat{p}_j^{\theta *} + E_j^{\varphi}\, \hat{p}_j^{\varphi *}, \tag{70}$$

$$F_j^{\mathrm{cx}} = \left|E_j^{\mathrm{cx}}\right|^2, \qquad E_j^{\mathrm{cx}} = E_j^{\theta}\, \hat{q}_j^{\theta *} + E_j^{\varphi}\, \hat{q}_j^{\varphi *}, \tag{71}$$

$$F_j^{\mathrm{tot}} = \left|E_j^{\theta}\right|^2 + \left|E_j^{\varphi}\right|^2, \tag{72}$$

where $\hat{\boldsymbol{p}}_j = \hat{\boldsymbol{p}}(\hat{\boldsymbol{r}}_j)$, $\hat{\boldsymbol{q}}_j = \hat{\boldsymbol{q}}(\hat{\boldsymbol{r}}_j)$, and the elements E_j^{θ} and E_j^{ϕ} may be evaluated exploiting fast matrix-vector product routines through (14)–(15).

We observe that one often seeks to maximize the gain in the main lobe, i.e., without a specification of an absolute lower bound for it. This is simply obtained by setting the lower bound M_0 to a theoretical maximum for the antenna under consideration, e.g., the value that would be obtained by a constant current and assuming the radiated power equal to the incident one. We also observe that in a pencil beam type of design the upper bound $M_{\mathrm{U}}^{\mathrm{co}}$ is not present, with related simplification of the ML functional ρ^{co}. In addition, for this case a sensible choice of the averaging ML region Ω_0 allows to use only the functional ρ_{ref}.

D. Fast Computation of Gradient

Our formulation allows to effectively make use of fast algorithms also for the gradient computation. In particular, the quadratic form of the terms result in linear gradients, and the sum over all terms allows to isolate the computationally intensive parts and drastically reduce the number of matrix-vector products required.

Matrices and vectors introduced in the previous sections are complex. On the other hand, optimization algorithms usually deal with real vectors: we strive to keep all computations in the complex domain for numerical convenience, using the approach proposed in [41]. To this end, we define the *complex gradient* operator as follows. Consider a complex vector $\mathsf{z} = \mathsf{x} + \mathrm{j}\mathsf{y} \in \mathbb{C}^N$. The complex gradient is defined as

$$\tilde{\nabla} \equiv \frac{1}{2}\big(\nabla_{\mathsf{x}} + \mathrm{j}\nabla_{\mathsf{y}}\big). \tag{73}$$

For a real-valued function $f : \mathbb{C}^N \to \mathbb{R}$, it can be proven [41] that: *i)* the complex gradient $\tilde{\nabla} f$ corresponds to the direction of maximum increase of the function; *ii)* the condition $\tilde{\nabla} f = 0$ is necessary and sufficient to determine a stationary point for f. The required gradients are expressed in complex format by using the properties reported in App. B, yielding

$$\tilde{\nabla} P_i = \frac{1}{2}\left(\mathbf{\Gamma}_i \mathsf{V} + \mathbf{K}^{\mathsf{H}} \mathbf{\Gamma}_i \mathsf{I}\right) \tag{74}$$

$$\tilde{\nabla} Q_i = \frac{1}{2\mathrm{j}}\left(\mathbf{\Gamma}_i \mathsf{V} - \mathbf{K}^{\mathsf{H}} \mathbf{\Gamma}_i \mathsf{I}\right) \tag{75}$$

$$\tilde{\nabla} \mathcal{J}_i = \frac{1}{2}\left(\mathbf{\Gamma}_i + \mathbf{\Gamma}_i^{\mathsf{H}}\right) \mathsf{I} = \mathbf{\Gamma}_i \mathsf{I} \tag{76}$$

$$\tilde{\nabla} \mathcal{E}_i = \mathbf{K}^{\mathsf{H}} \mathbf{\Gamma}_i \mathsf{V}, \tag{77}$$

where the matrix $\mathbf{K}$ was defined in (54), and the products involving it are computed in the following way:

$$\mathbf{K}^{\mathsf{H}} \mathsf{z} = (\mathbf{G}^{-1} \mathbf{L})^{\mathsf{H}} \mathsf{z} = \mathbf{L}^{\mathsf{H}} \mathbf{G}^{-1} \mathsf{z}, \tag{78}$$

having exploited the symmetry of $\mathbf{G}^{-1}$. We observe that the EFIO matrix $\mathbf{L}$ is symmetric, i.e., $\mathbf{L}^{\mathsf{T}} = \mathbf{L}$, but not self-adjoint. Thus, matrix-vector products involving its complex transpose are computed as

$$\mathbf{L}^{\mathsf{H}} \mathsf{z} = (\mathbf{L}^{\mathsf{T}} \mathsf{z}^*)^* = (\mathbf{L} \mathsf{z}^*)^* \tag{79}$$

which allows to leverage fast algorithms to multiply $\mathbf{L}$ by a vector. The total gradient is obtained by linearity as a sum of all individual gradients. As an example, the gradient of the ρ_{act} functional is given by

$$\begin{aligned} \tilde{\nabla}\Big[\textstyle\sum_i {P_i}^2\Big] &= 2 \textstyle\sum_i P_i \tilde{\nabla} P_i \\ &= 2 \textstyle\sum_i P_i \, \tfrac{1}{2}\big(\mathbf{\Gamma}_i \mathsf{V} + \mathbf{K}^{\mathsf{H}} \mathbf{\Gamma}_i \mathsf{I}\big) \\ &= \Big[\textstyle\sum_i P_i \mathbf{\Gamma}_i \mathsf{V}\Big] + \mathbf{K}^{\mathsf{H}} \Big[\textstyle\sum_i P_i \mathbf{\Gamma}_i \mathsf{I}\Big] \end{aligned} \tag{80}$$

The interchange of the summation with the operator $\mathbf{K}^{\mathsf{H}}$ is key as it allows to compute the total gradient by requiring only one computationally intensive matrix-vector product. The remaining products, involving extremely sparse matrices $\mathbf{\Gamma}_i$, are computed individually, as their complexity remains negligible with respect to the total one.

The same is true for the inequality terms; in the case of ρ_{rct}, by defining $\Psi_i = Q_i - X \mathcal{J}_i$ and noting that $\frac{\mathrm{d}}{\mathrm{d}x}\mathrm{r}^2(x) = 2\,\mathrm{r}(x)$, we have

$$\begin{aligned} \tilde{\nabla} \Psi_i &= \tilde{\nabla} Q_i - X \tilde{\nabla} \mathcal{J}_i \\ &= \frac{1}{2\mathrm{j}}\left(\mathbf{\Gamma}_i \mathsf{V} - \mathbf{K}^{\mathsf{H}} \mathbf{\Gamma}_i \mathsf{I}\right) - X \mathbf{\Gamma}_i \mathsf{I} \\ &= \frac{1}{2}\big(- \mathrm{j} \mathbf{\Gamma}_i \mathsf{V} + (\mathrm{j}\mathbf{K}^{\mathsf{H}} - 2X) \mathbf{\Gamma}_i \mathsf{I}\big) \end{aligned} \tag{81}$$

and so

$$\begin{aligned} &\tilde{\nabla}\Big[\textstyle\sum_i \mathrm{r}^2(\Psi_i)\Big] = 2 \textstyle\sum_i \mathrm{r}(\Psi_i) \tilde{\nabla} \Psi_i \\ &= -\mathrm{j}\Big[\textstyle\sum_i \mathrm{r}(\Psi_i) \mathbf{\Gamma}_i \mathsf{V}\Big] + (\mathrm{j}\mathbf{K}^{\mathsf{H}} - 2X)\Big[\textstyle\sum_i \mathrm{r}(\Psi_i) \mathbf{\Gamma}_i \mathsf{I}\Big]. \end{aligned} \tag{82}$$

Regarding the functional for the field specifications, the gradients of the field magnitude samples read

$$\tilde{\nabla} F_j^{\mathrm{co}} = E_j^{\mathrm{co}} (\hat{p}_{\theta j} \mathbf{R}_{\theta}^{\mathsf{H}} \mathsf{e}_j + \hat{p}_{\phi j} \mathbf{R}_{\phi}^{\mathsf{H}} \mathsf{e}_j) \tag{83}$$

$$\tilde{\nabla} F_j^{\mathrm{cx}} = E_j^{\mathrm{cx}} (\hat{q}_{\theta j} \mathbf{R}_{\theta}^{\mathsf{H}} \mathsf{e}_j + \hat{q}_{\phi j} \mathbf{R}_{\phi}^{\mathsf{H}} \mathsf{e}_j) \tag{84}$$

$$\tilde{\nabla} F_j^{\mathrm{tot}} = E_j^{\theta}\, \mathbf{R}_{\theta}^{\mathsf{H}} \mathsf{e}_j + E_j^{\varphi}\, \mathbf{R}_{\varphi}^{\mathsf{H}} \mathsf{e}_j \tag{85}$$

where $(\mathsf{e}_j)_k = \delta_{jk}$. The gradient for the total field component in (66) is found in a way similar to what has been shown before. By defining $\Phi_j = F_j^{\mathrm{tot}} - M_{\mathrm{U},j}^{\mathrm{tot}}$, we get

$$\begin{aligned}\tilde{\nabla}\Phi_j &= \tilde{\nabla}F_j^{\mathrm{tot}} - \tilde{\nabla}M_{\mathrm{U},j}^{\mathrm{tot}}\\ &= \tilde{\nabla}F_j^{\mathrm{tot}} = E_j^{\theta}\,\mathsf{R}_{\theta}^{\mathsf{H}}\mathsf{e}_j + E_j^{\varphi}\,\mathsf{R}_{\varphi}^{\mathsf{H}}\mathsf{e}_j\end{aligned} \tag{86}$$

where the simplifying assumption of absolute masks, i.e., $\tilde{\nabla}M_{\mathrm{U},j}^{\mathrm{tot}} = 0$, has been made. Then

$$\begin{aligned}\tilde{\nabla}\Big[\textstyle\sum_j \mathrm{r}^2(\Phi_j)\Big] &= 2\textstyle\sum_j \mathrm{r}(\Phi_j)\tilde{\nabla}\Phi_j\\ &= 2\textstyle\sum_j \mathrm{r}(\Phi_j)\big[E_j^{\theta}\,\mathsf{R}_{\theta}^{\mathsf{H}}\mathsf{e}_j + E_j^{\varphi}\,\mathsf{R}_{\varphi}^{\mathsf{H}}\mathsf{e}_j\big]\\ &= \mathsf{R}_{\theta}^{\mathsf{H}}\Big[2\textstyle\sum_j \mathrm{r}(\Phi_j)E_j^{\theta}\mathsf{e}_j\Big] + \mathsf{R}_{\varphi}^{\mathsf{H}}\Big[2\textstyle\sum_j \mathrm{r}(\Phi_j)E_j^{\varphi}\mathsf{e}_j\Big]\end{aligned} \tag{87}$$

where again, by rearranging the summation, the computationally heavy matrix-vector products are done only once per gradient evaluation.

E. Iteration update

As anticipated, for the minimization of the functional $f(\mathsf{l})$ described in previous sections we employ a *non-linear conjugate gradient* algorithm [39, p. 121]; this means that the update is of the type

$$\mathsf{l}_{k+1} = \mathsf{l}_k + \alpha_k\,\mathsf{p}_k \tag{88}$$

with $k = 0, \ldots, K_{\max}$, where $\alpha_k \in \mathbb{R}$ is to be found so that the functional is minimized along the direction $\mathsf{p}_k \in \mathbb{C}^N$, which incorporates gradient information,

$$\mathsf{p}_k = \begin{cases} -\tilde{\nabla}f_k & \text{if } k = 0\\ -\tilde{\nabla}f_k + \beta_k\,\mathsf{p}_{k-1} & \text{if } k > 0\end{cases} \tag{89}$$

The parameter $\beta \in \mathbb{R}$ is defined according to the Polak-Ribière formula (adapted for complex gradients),

$$\beta_k = \frac{\mathrm{Re}\left(\tilde{\nabla}f_k^{\mathsf{H}}(\tilde{\nabla}f_k - \tilde{\nabla}f_{k-1})\right)}{\left\|\tilde{\nabla}f_{k-1}\right\|^2} \tag{90}$$

As seen above, at each iteration of the algorithm, one updates the solution by looking for the optimum along the chosen direction; this step is known as *line search*, and is formally indicated as the process of finding the optimum step length $\alpha^{\star}$ such that:

$$\alpha^{\star} = \underset{\alpha\in\mathbb{R}}{\arg\min}\, f(\mathsf{l} + \alpha\,\mathsf{p}) \tag{91}$$

where l indicates the solution at the previous step (i.e., $\mathsf{l} = \mathsf{l}_k$) and $\mathsf{p} = \mathsf{p}_k$ is the search direction as in (89). As the line search is performed at each iteration, its computational cost is of paramount importance. Both the evaluation of the cost function along the search direction,

$$g(\alpha) = f(\mathsf{l} + \alpha\,\mathsf{p}) \tag{92}$$

and the minimization process are greatly expedited by our choice to employ only polynomial functionals (see Sec. IV-A). First of all, we make explicit the polynomial structure of each term in (35) when evaluated in (92):

$$q_d(\mathsf{l} + \alpha\,\mathsf{p}) = q_{0d} + \alpha\,q_{1d} + \alpha^2 q_{2d} \tag{93}$$

with

$$q_{0d} = \mathrm{Re}(\mathsf{l}^{\mathsf{H}}\mathbf{\mathsf{A}}_d\mathsf{l} + \mathsf{l}^{\mathsf{H}}\mathsf{b}_d + c_d) \tag{94}$$

$$q_{1d} = \mathrm{Re}(\mathsf{l}^{\mathsf{H}}\mathbf{\mathsf{A}}_d\mathsf{p} + \mathsf{p}^{\mathsf{H}}\mathbf{\mathsf{A}}_d\mathsf{l} + \mathsf{p}^{\mathsf{H}}\mathsf{b}_d) \tag{95}$$

$$q_{2d} = \mathrm{Re}(\mathsf{p}^{\mathsf{H}}\mathbf{\mathsf{A}}_d\mathsf{p}) \tag{96}$$

where $\mathbf{\mathsf{A}}_d$ indicate the matrices appearing in the definition of the objective function terms. The same applies to the imaginary part. By defining the arrays of coefficients $\mathsf{q}_0 = [\cdots q_{0d}\cdots]^{\mathsf{T}}$, $\mathsf{q}_1 = [\cdots q_{1d}\cdots]^{\mathsf{T}}$ and $\mathsf{q}_2 = [\cdots q_{2d}\cdots]^{\mathsf{T}}$ (and, accordingly, for the polynomials s_d and t_d), we can conveniently evaluate (92) as

$$\begin{aligned}g(\alpha) = {}&(\mathsf{q}_0 + \alpha\,\mathsf{q}_1 + \alpha^2\mathsf{q}_2)^{\mathsf{T}}(\mathsf{s}_0 + \alpha\,\mathsf{s}_1 + \alpha^2\mathsf{s}_2)\\ &+ \mathrm{r}(\mathsf{t}_0 + \alpha\,\mathsf{t}_1 + \alpha^2\mathsf{t}_2)^{\mathsf{T}}\mathrm{r}(\mathsf{t}_0 + \alpha\,\mathsf{t}_1 + \alpha^2\mathsf{t}_2).\end{aligned} \tag{97}$$

This formulation allows to evaluate the objective function (92) for *any* value of α at the cost of computing the matrix-vector products involving $\mathbf{\mathsf{A}}_d$ only once to evaluate $\mathbf{\mathsf{A}}_d\mathsf{p}$, as terms $\mathbf{\mathsf{A}}_d\mathsf{l}$ were computed and stored at the previous step.

Moreover, an analytical solution for the minimization of $g(\alpha)$ is important to avoid scaling issues of the step length, which is known to be a critical problem of line search procedures [39]. We discuss this by starting with the simplest case of functionals without inequalities (i.e., without ramp functions); in our setting, that would correspond to a phaseless pattern fitting with no bounds on the reactance values. In this case, the objective function $g(\alpha)$ reduces to a fourth-order polynomial and the line search procedure is direct: the derivative $\frac{\mathrm{d}g}{\mathrm{d}\alpha}$ is a third-order polynomial, and its roots may be found in closed form. Once again, we stress that this is not important to reduce the cost of finding the stationary point. Instead, a closed form solution avoids the need to determine the interval in which to look for the optimum step length.

In the presence of inequalities, the objective $g(\alpha)$ is still a fourth-order polynomial, but it is piecewise so; because of the continuity of the derivative of $\mathrm{r}^2(x)$, the derivative $\frac{\mathrm{d}g}{\mathrm{d}\alpha}$ is also a piecewise continuous polynomial. The piecewise polynomial (97) can be minimized with an iterative algorithm, that can be explained as follows: note that, for a generic function $\phi(x)$, we have

$$\mathrm{r}(\phi(x)) = \mathrm{u}(\phi(x))\,\phi(x), \tag{98}$$

where $\mathrm{u}(x)$ is the unit step function; hence, the non-linear (rectifying) behavior of a ramp can be represented as an on/off switch. Then, we consider the ramp-less "switched" version $g^{\mathrm{s}}(\alpha;\mathsf{u})$ of (97) in which all terms of the kind $\mathrm{r}(s_d(\alpha))$ are replaced by $u_d\,s_d(\alpha)$, with $u_d = \mathrm{u}(s_d(\alpha)) \in \{0, 1\}$ and where $\mathsf{u} = [u_1, \ldots, u_{N_{\mathrm{s}}}]$ is the switch pattern vector (N_{s} is the number of switches, i.e., of ramp terms). For any given pattern of switch states, the function $g^{\mathrm{s}}(\alpha;\mathsf{u})$ is always a fourth-order polynomial whose minimum point is computed in closed form as described above.

One starts by computing the switch pattern for $\alpha = 0$, which yields u_0, and finds the minimum $\alpha_0^{\star}$ of $g^{\mathrm{s}}(\alpha;\mathsf{u}_0)$ as above. With this new value of α, one now evaluates the switches again, which results in the pattern u_1, and the determination of the minimum point is repeated for $g^{\mathrm{s}}(\alpha;\mathsf{u}_1)$, yielding $\alpha_1^{\star}$. The process is iterated until the switch pattern remains unchanged,

This article has been accepted for publication in IEEE Transactions on Antennas and Propagation. This is the author's version which has not been fully edited and content may change prior to final publication. Citation information: DOI 10.1109/TAP.2023.3270715

TABLE I
COMPUTATIONAL COMPLEXITY OF REQUIRED MATRIX-VECTOR OPERATIONS, WITH THE TOTAL NUMBER OF OCCURRENCES PER ITERATION.

Operation	Complexity	Count
$\mathbf{\mathsf{L}}\mathsf{I}$	$O(N\log N)$	3
$\mathbf{\mathsf{R}}\mathsf{I}$	$O(N_{\mathrm{f}}\log N)$	3
$\mathbf{\mathsf{G}}^{-1}\mathsf{I}$	$O(N)$	3
$\mathbf{\Gamma}_i\,\mathsf{I}$	$O(1)$	$4N_{\mathrm{c}}$

i.e., $\mathsf{u}_n = \mathsf{u}_{n-1}$: at that point, $g^{\mathrm{s}}(\alpha;\mathsf{u}_n) = g(\alpha)$, and $\alpha_n^\star = \alpha^\star$ is the sought-for minimum point. The algorithm usually converges in much less than N_{s} iterations.

F. Computational complexity

The computation of the objective function and of its gradient consists of operations that are amenable to at most $O(N\log N)$ complexity and $O(N)$ memory occupation. In particular, the matrix-vector products $\mathbf{\mathsf{L}}\mathsf{I}$ and $\mathbf{\mathsf{R}}\mathsf{I}$ can be computed with fast factorizations as described in Sec. II, while terms of the kind $\mathsf{y} = \mathbf{\mathsf{G}}^{-1}\mathsf{x}$ are evaluated directly as solutions of the linear system $\mathbf{\mathsf{G}}\,\mathsf{y} = \mathsf{x}$. The Gram matrix is $O(N)$ sparse, positive-definite and with $O(1)$ condition number, therefore the above system can be solved iteratively (e.g., with a conjugate gradient algorithm) in $O(1)$ iterations, thus resulting in $O(N)$ total operations.

Table I summarizes the complexity of all matrix-vector operations; the total count includes all operations needed for the evaluation of the objective function, of its gradient, and for the line-search. Given that the number of sampling points in the far field, N_{f}, is independent of the number of unknowns N, and the number of cells N_{c} is approximately proportional to N, the total asymptotic complexity (neglecting multiplicative constants) is $O(N\log N)$. In this estimation, element-wise vector operations have been omitted since their cost is negligible with respect to matrix-vector ones.

G. From current to impedance

Once the optimum current coefficients $\mathsf{I}^\star$ have been obtained, the corresponding total electric field $\mathsf{V}_{\mathrm{inc}} + \mathbf{\mathsf{L}}\mathsf{I}^\star$ is also known, and the sought-for impedance profile can be obtained via (7) and the definition of $\mathbf{\mathsf{Z}}$ (9).

In order to find an equation for the impedance spatial distribution $Z(\boldsymbol{r})$ we must start with its representation in terms of L assigned basis functions $\psi_\ell(\boldsymbol{r})$,

$$Z(\boldsymbol{r}) = \sum_{\ell=1}^{L} z_\ell\,\psi_\ell(\boldsymbol{r}), \tag{99}$$

where the array $\mathsf{z} \in \mathbb{C}^L$ collects the expansion coefficients. We observe that this step—including the choice of the impedance basis functions—is completely independent from the solution of the optimization process described above, and any post-processing to it. Indeed, more than one representations of $Z(\boldsymbol{r})$ and ensuing impedance reconstructions could be done for ensuring a stable result. Inserting (99) into (9), one has

$$(\mathbf{\mathsf{Z}})_{mn} = \sum_{\ell=1}^{L} z_\ell\, g_{mn}^{\ell}, \quad g_{mn}^{\ell} = \langle\, \mathbf{\Lambda}_m \,, \psi_\ell \mathbf{\Lambda}_n \,\rangle, \tag{100}$$

and after some manipulations, one finds

$$\mathbf{\mathsf{Z}}\mathsf{I} = \mathbf{\mathsf{C}}\mathsf{z}, \quad \mathbf{\mathsf{C}}(\mathsf{I}) \in \mathbb{C}^{N\times L}, \quad (\mathbf{\mathsf{C}})_{m\ell} = \sum_{n=1}^{N} g_{mn}^{\ell} I_n \tag{101}$$

Consistency with the discretized EFIE-IBC (7) (with known current $\mathsf{I} = \mathsf{I}^\star$) requires

$$\mathbf{\mathsf{C}}^\star \mathsf{z} = \mathsf{V}_{\mathrm{inc}} + \mathbf{\mathsf{L}}\mathsf{I}^\star \tag{102}$$

with $\mathbf{\mathsf{C}}^\star = \mathbf{\mathsf{C}}(\mathbf{\mathsf{I}}^\star)$, so that

$$\mathsf{z}^\star = \underset{\mathsf{z}\,\in\,\mathbb{C}^L}{\arg\min} \left\| \mathbf{\mathsf{C}}^\star \mathsf{z} - \mathsf{V}_{\mathrm{inc}} - \mathbf{\mathsf{L}}\mathsf{I}^\star \right\|^2 \tag{103}$$

which corresponds to a linear, least-squares minimization problem that can be solved with standard techniques. We observe that this process bears similarities with the impedance computation in [16]. In what follows, we expand the sought impedance profile with piecewise constant basis functions

$$\psi_\ell(\boldsymbol{r}) = \begin{cases} 1 & \text{for } \boldsymbol{r} \in \overline{\mathcal{S}}_\ell \\ 0 & \text{elsewhere} \end{cases} \qquad \ell = 1,\ldots,L \tag{104}$$

where $\overline{\mathcal{S}}_\ell$, in general, is given by the union of a certain number of adjacent triangular cells. This can help in smoothing out fast variations of the impedance profile, or to more closely match the unit cell shape.

In the particular case in which the impedance is expanded with constant basis functions on each triangle separately, $L = N_{\mathrm{c}}$, $\overline{\mathcal{S}}_i = \mathcal{S}_i$, and problem (103) has a closed form solution for the impedance coefficients (derived in App. C), given by

$$z_i^\star = \frac{\mathsf{I}^{\mathsf{H}} \mathbf{\Gamma}_i \mathsf{V}}{\mathsf{I}^{\mathsf{H}} \mathbf{\Gamma}_i \mathsf{I}}. \tag{105}$$

Extension to the case of clusters of cells is straightforward.

We observe that two relevant limiting cases can be encountered. When the total field $\boldsymbol{E}$ in (3) is zero and the current $\boldsymbol{J}$ is not, the surface is a PEC (equivalent to $Z = 0$). Instead, when the current $\boldsymbol{J}$ is zero and the field $\boldsymbol{E}$ is not, this corresponds to an infinite impedance value, which implies that there is *no IBC* there (i.e., only the dielectric substrate), a condition that can be easily implemented in the solution by removing the corresponding degrees of freedom from the discretization. In practice, thresholds are set for the current and field values, defining how small the quantities must be in order to be considered negligible.

Finally, we note that sensitivity may arise due to the current at the denominator, or more generally because current and impedance appear as a product in (7). Handling the above limiting cases avoids most of the problems, but further regularization processes may be necessary to yield smoother profiles; in this sense, we note that smoothing the current would not necessarily solve the above sensitivity issues, which may still happen even for a very smooth current profile.

This article has been accepted for publication in IEEE Transactions on Antennas and Propagation. This is the author's version which has not been fully edited and content may change prior to final publication. Citation information: DOI 10.1109/TAP.2023.3270715

V. APPLICATION EXAMPLES

In this section, the proposed algorithm is applied to the design of metasurface antennas with different shapes. This paper is devoted to the design of the *impedance surface*. The design of the feed, or inclusion of a realistic feed model are beyond the present scope. Hence, as in similar works (e.g., [16]) we will consider excitation by (one or more) vertical pins. This is not a limitation, as more realistic feeds may be incorporated via their incident field $\boldsymbol{E}_{\text{inc}}$ (e.g., [42]).

The first case is a circular metasurface radiating a broadside pencil beam with circular and linear polarization, while the second case involves a rectangular metasurface that radiates a cosecant squared pattern.

In all cases we required a capacitive-only reactance (which greatly simplifies unit cell design), with values in the range from $-600\,\Omega$ to $-100\,\Omega$ (which are typical for patch-type unit cells with the employed substrate and frequency).

All reported examples incorporated the requirement of *realized gain maximization* (for fixed unit incident power). We recall that the optimization process avoids the solution of the forward problem (7); this fact will be used to verify the consistency and stability of the obtained impedance profile. We proceed as follows: from the optimum current $\mathsf{I}^\star$, we determine the impedance profile $Z(\boldsymbol{r})$ as indicated in Sec. IV-G, keeping only its imaginary part. Next, we compute the actual solution by solving the forward problem (7) for this impedance profile and the specified source field.

All the radiation patterns shown have been obtained this way; hence, the results take into account a possible efficiency reduction due to the impedance reconstruction process. Losses in the conductors and the dielectric substrate are not considered. In obtaining the impedance, as described in Sec. IV-G, currents below the threshold were neglected. In all the examples, this threshold corresponds to 2% of the average current magnitude.

Employed mask specifications will be graphically reported along with results. In surface impedance plots, white areas are used to represent an open circuit condition, i.e., where only the bare dielectric substrate is present.

The design instances ran on a Desktop PC with Intel Core i7 processor and $16\,\text{GB}$ RAM.

A. Circular Metasurface with Broadside Pencil Beam

The first application considers a circular structure, given the practical relevance of this configuration in the literature. The antenna has a diameter $D = 130\,\text{mm} \approx 20\lambda_0$ ($\lambda_0 = c/f$), it features $N_\text{c} = 61\,594$ degrees of freedom for the impedance, and is discretized with $N = 92\,096$ RWG basis functions. The substrate is a single-layer grounded dielectric slab with $\varepsilon_\text{r} = 3.34$ and height $h = 0.508\,\text{mm}$; the operation frequency is $23\,\text{GHz}$. The incident field is generated by a (short) centered vertical dipole, and approximated with its asymptotic form as a TM_0 cylindrical surface wave (as in, e.g., [26]); its associated power (i.e., the incident power) can be computed in a straightforward manner [43], and setting it to a given value (e.g., unitary) yields the amplitude of this surface wave.

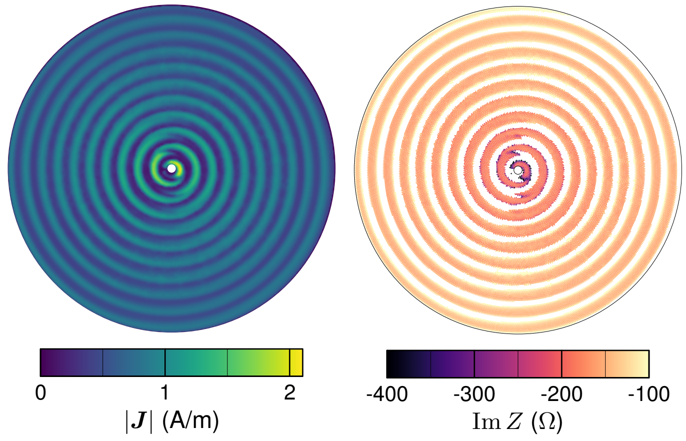

(a) (b)

Fig. 3. Pencil beam with circular polarization: (a) optimized surface current magnitude, (b) resulting surface reactance (white areas correspond to the absence of IBC, i.e., bare dielectric).

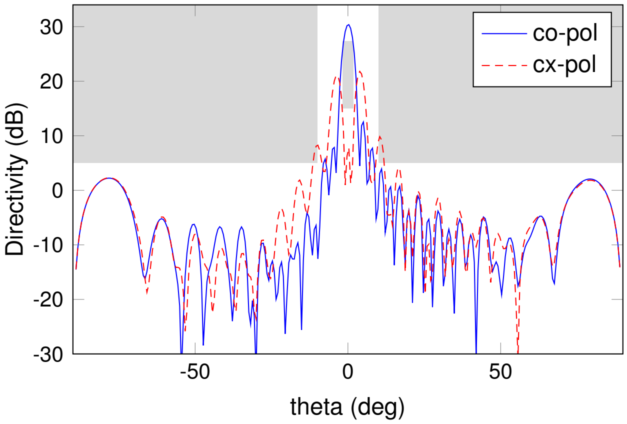

Fig. 4. Pencil beam pattern with circular polarization: mask requirements and directivity in the plane cut $\varphi = 90^\circ$.

The current is initialized to an everywhere $\hat{\boldsymbol{y}}$-directed current with a raised-cosine radial profile with roll-off toward the inner and outer edges, which radiates *broadside* with *linear polarization*. This current is (obviously) not realizable with a passive lossless metasurface, and this will allow to assess the robustness of the algorithm with respect to the starting point.

The optimization of the circular metasurface took 500 iterations, each requiring $\approx\ 50\,\text{s}$ to complete, for a total running time of about $7\,\text{h}$ for each presented case.

1) Circular polarization: We begin with a pencil beam design with circular polarization. The output of the optimization is the surface current in Fig. 3a, with the corresponding impedance shown in Fig. 3b.

Figures 4 shows the requirement masks (with azimuthal symmetry) along with the obtained patterns. A view of the pattern in the u-v plane is also given in Fig. 7a. The maximum directivity is $30.3\,\text{dB}$, with a corresponding aperture efficiency of 28%; this value is in line with those reported in the literature for scalar impedances, which range between 15% and 20% [2].

It is remarkable that the proposed optimization algorithm reaches the same spiral shape that was devised in [2] based

This article has been accepted for publication in IEEE Transactions on Antennas and Propagation. This is the author's version which has not been fully edited and content may change prior to final publication. Citation information: DOI 10.1109/TAP.2023.3270715

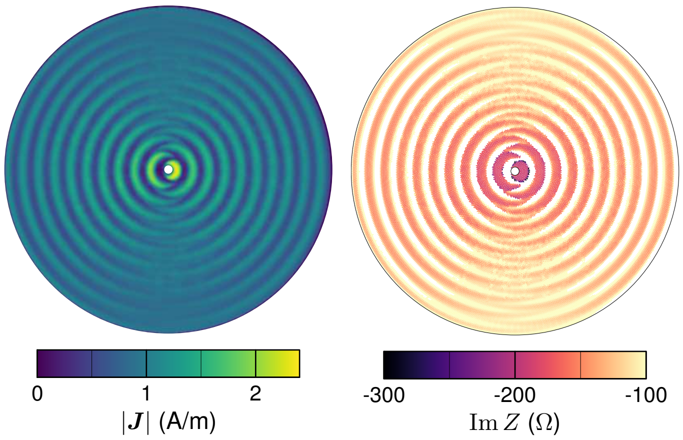

(a) (b)

Fig. 5. Pencil beam with linear polarization: (a) optimized surface current magnitude, (b) resulting surface reactance (white areas correspond to the absence of IBC, i.e., bare dielectric).

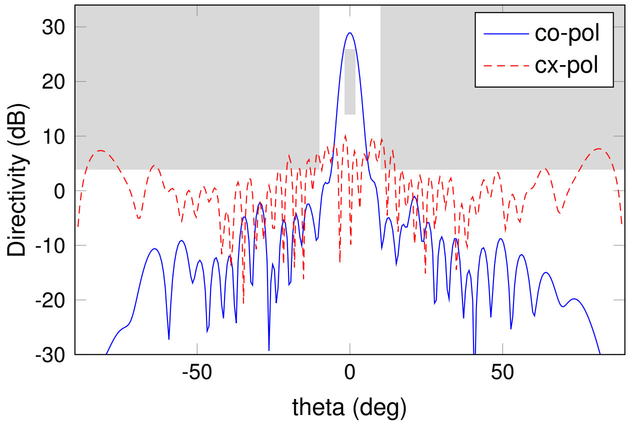

Fig. 6. Pencil beam pattern with linear polarization: mask requirements and directivity in the plane cut $\varphi = 90°$.

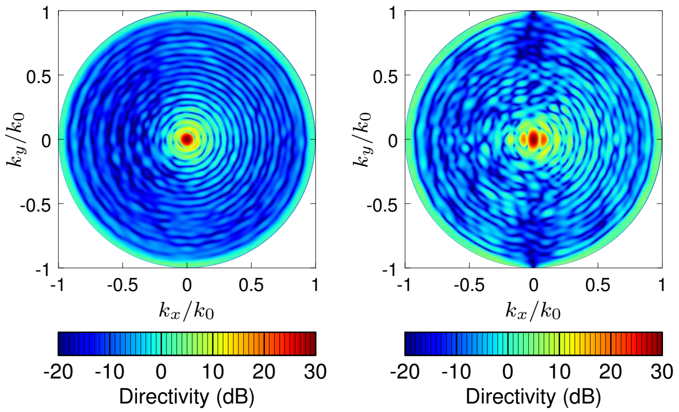

(a) (b)

Fig. 7. Comparison of the co-polarization patterns in the u-v plane for (a) circular polarization and (b) linear polarization broadside pencil beam.

on analytical considerations, and the one obtained with the current-only method [16] employing entire-domain basis functions; the proposed algorithm employs no assumption, and actually reaches this spiral profile and circular polarization starting from a constant current with linear polarization.

2) Linear polarization: We now address the case of linear polarization, which is less usual for the considered type of antenna. As the antenna has a circular symmetry, and our focus is on broad-side radiation, there is no difference in design between the vertical and horizontal polarizations. The optimized current and surface reactance are shown in Fig. 5a and 5b.

The (axi-symmetric) mask specifications for this case are in Fig. 6 along with the obtained radiated field. A plot of the pattern in the u-v plane is given in Fig. 7b. The directivity reaches a maximum of 28.8 dB, achieving a 20% aperture efficiency. Side-lobe performance appear different in the E- and H-plane, and worse in the E-plane with respect to the circular polarization case. This difference can be attributed to the scalar impedance employed here.

The resulting impedance distribution shows clear similarities with that of [44], obtained as the superposition of two spiral modulation patterns that radiate opposite circularly polarized beams. The work in [3], [45] include broadside-radiation cases, albeit for tensor impedance. Hence, analogous to the circular polarization case, it is remarkable that our automated design recovers a shape determined on the basis of analytical wave-based considerations.

Further application examples, notably for smaller sized antennas and flat-top patterns, can be found in [46]; as for the aperture efficiency, a $10\lambda_0$ circular antenna radiating a circularly polarized broadside beam showed an aperture efficiency of 35%, while for the linearly polarized case this efficiency reached 40%.

B. Rectangular Metasurface with Cosecant Squared Pattern

The second application features a rectangular metasurface at 32 GHz, with a length $L = 93.7\,\mathrm{mm} \approx 20\lambda_0$ and a width $W = 65.6\,\mathrm{mm} \approx 7\lambda_0$. The impedance is discretized with $N_\mathrm{c} = 24\,288$ degrees of freedom and the number of RWG basis functions for the current is $N = 36\,136$. A grounded dielectric slab with $\varepsilon_\mathrm{r} = 3.0$ and height $h = 0.76\,\mathrm{mm}$ serves as the substrate. The antenna is excited by a row of pins placed in a rectangular quiet zone at the center of antenna with a cosine tapering, which produces a surface wave with an almost plane wavefront along the width of the metasurface.

The target specification is a *cosecant squared* pattern, tipically encountered in applications that need a constant radiated angular power density over a defined range of elevation angles θ, and null outside [40]. The power pattern $D(\theta)$ is defined as

$$D(\theta) = \frac{\sin^2(\theta_\mathrm{min})}{\sin^2(\theta)}, \quad \theta_\mathrm{min} \le \theta \le \theta_\mathrm{max}. \tag{106}$$

In the following, we will consider a case with $\theta_\mathrm{min} = 5°$, $\theta_\mathrm{max} = 50°$ and linear polarization along $\hat{\boldsymbol{\theta}}$. The principal plane here is $\phi = 0°$, and radiation constraints are imposed in this plane. The admissible ripple is set at $\pm 2\,\mathrm{dB}$ from the target mask (106), and the transition zone is 5° on both sides of the main beam. Unsymmetrical sidelobe requirements are set on the two sides.

This article has been accepted for publication in IEEE Transactions on Antennas and Propagation. This is the author's version which has not been fully edited and content may change prior to final publication. Citation information: DOI 10.1109/TAP.2023.3270715

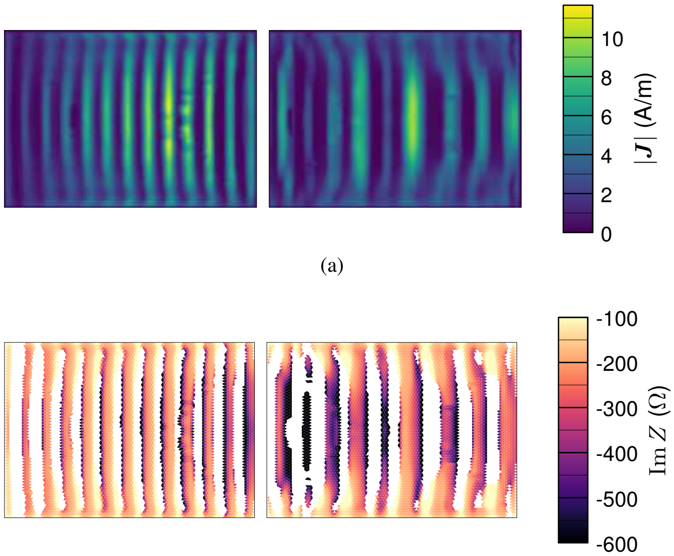

(a)

(b)

Fig. 8. Cosecant squared pattern: (a) optimized surface current magnitude, (b) resulting surface reactance (white areas correspond to the absence of IBC, i.e., bare dielectric).

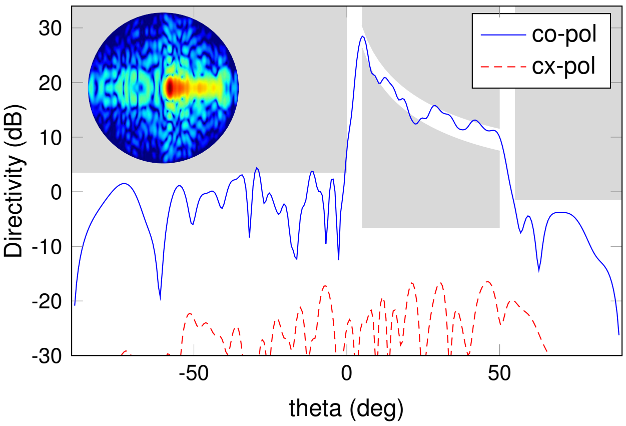

Fig. 9. Cosecant squared pattern: mask requirements and directivity in the plane cut $\varphi = 0°$. Inset: co-polarization directivity pattern in the u-v plane.

Figure 8a shows the optimized current, and the corresponding surface impedance is given in Fig. 8b. The optimized radiated pattern is displayed in Fig. 9, together with the specification mask.

To obtain the final design, 2000 iterations were carried out, with an average of $\approx 10\,\mathrm{s}$ per iteration, and a total runtime of around $5\,\mathrm{h}\,30\,\mathrm{min}$.

VI. CONCLUSIONS

We have presented a 3D method to numerically design metasurfaces antennas which transform a given incident field into a radiated one with arbitrary mask-type (inequality) amplitude specifications, and with bounds on the surface reactance values. The method employs only the (equivalent) electric current, not requiring the solution of the forward problem at each iteration, thus allowing for a reduced computational cost. The problem is further cast so as to allow the use of fast matrix-vector product routines, reaching an almost-linear complexity.

Inclusion of realistic feed models is currently underway, and preliminary results are reported in [42]. Generalization to tensor impedance and dual-polarization will be the first natural extensions of this work. Current and impedance smoothing will also be considered in the future.

APPENDIX A
ENERGY BALANCE ACROSS THE METASURFACE

In order to define the energetic properties of a metasurface, we need to find the expression of the absorbed power density for a surface $\mathcal{S}$. To this aim, we apply Poynting's theorem to an arbitrary volume $\mathcal{V}$ that crosses this surface, giving

$$\begin{aligned}\tilde{P} &= P_{\mathrm{diss}} + \mathrm{j}2\omega(W_{\mathrm{m}} - W_{\mathrm{e}})\\ &= \iiint_{\mathcal{V}} \tilde{p}\;\mathrm{d}V = \oiint_{\partial\mathcal{V}} \boldsymbol{S}\cdot\hat{\boldsymbol{n}}\,\mathrm{d}S\end{aligned} \tag{107}$$

where P_{diss} is the total dissipated power, W_{m} and W_{e} are the magnetic and electric stored energies, respectively, and $\tilde{p}$ is the absorbed (volume) power density. The surface integral involves the Poynting vector $\boldsymbol{S} = \boldsymbol{E}\times\boldsymbol{H}^*$ and the normal unit vector $\hat{\boldsymbol{n}}$ is directed inside the volume, as dictated by the "load" convention. The boundary $\partial\mathcal{V}$ is given by the union of three disjoint surfaces: $\mathcal{S}_+$ and $\mathcal{S}_-$ are on the opposite sides of $\mathcal{S}$, while $\mathcal{S}_{\mathrm{side}}$ is the surface that joins the two sides across $\mathcal{S}$. With this partition of the bounding surface, the surface integral can be written as

$$\tilde{P} = \iint_{\mathcal{S}_+} \boldsymbol{S}\cdot\hat{\boldsymbol{n}}\,\mathrm{d}S + \iint_{\mathcal{S}_-} \boldsymbol{S}\cdot\hat{\boldsymbol{n}}\,\mathrm{d}S + \iint_{\mathcal{S}_{\mathrm{side}}} \boldsymbol{S}\cdot\hat{\boldsymbol{n}}\,\mathrm{d}S \tag{108}$$

In the limit where $\mathcal{S}_+$ and $\mathcal{S}_-$ tend to $\mathcal{S}$ from the two sides, the volume integral collapses into a surface integral over $\mathcal{S}$ and the contribution of the integral over $\mathcal{S}_{\mathrm{side}}$ vanishes. The normal unit vectors on both sides have opposite directions, i.e., $\hat{\boldsymbol{n}}|_{\mathcal{S}_-} = -\hat{\boldsymbol{n}}|_{\mathcal{S}_+} \equiv \hat{\boldsymbol{n}}$, and the expression for the total surface power (107) reduces to

$$\lim_{\substack{\mathcal{S}_+\to\mathcal{S}\\ \mathcal{S}_-\to\mathcal{S}}} \tilde{P} = \iint_{\mathcal{S}} \tilde{p}\;\mathrm{d}S = -\iint_{\mathcal{S}} (\boldsymbol{S}_+ - \boldsymbol{S}_-)\cdot\hat{\boldsymbol{n}}\,\mathrm{d}S. \tag{109}$$

By restricting the analysis to the case where the surface introduces discontinuities in the magnetic field only (as is the case for a metasurface that is modelled by (1)), it follows that $\boldsymbol{E}_+ = \boldsymbol{E}_- = \boldsymbol{E}$ and the final expression reads

$$\begin{aligned}\tilde{P} &= \iint_{\mathcal{S}} \tilde{p}\;\mathrm{d}S = -\iint_{\mathcal{S}} \boldsymbol{E}\times(\boldsymbol{H}_+ - \boldsymbol{H}_-)^*\cdot\hat{\boldsymbol{n}}\,\mathrm{d}S\\ &= \iint_{\mathcal{S}} \boldsymbol{E}\cdot[\hat{\boldsymbol{n}}\times(\boldsymbol{H}_+ - \boldsymbol{H}_-)^*]\,\mathrm{d}S = \iint_{\mathcal{S}} \boldsymbol{E}\cdot\boldsymbol{J}^*\,\mathrm{d}S\end{aligned} \tag{110}$$

where we have used definition (2) for the equivalent surface current. Since the surface $\mathcal{S}$ is arbitrary, the equality of the integrands in (110) must hold point-wise. The definition of the surface absorbed power density is therefore given by

$$\tilde{p} = \boldsymbol{E}\cdot[\hat{\boldsymbol{n}}\times(\boldsymbol{H}_+ - \boldsymbol{H}_-)^*] = \boldsymbol{E}\cdot\boldsymbol{J}^*. \tag{111}$$

This article has been accepted for publication in IEEE Transactions on Antennas and Propagation. This is the author's version which has not been fully edited and content may change prior to final publication. Citation information: DOI 10.1109/TAP.2023.3270715

APPENDIX B
PROPERTIES OF THE COMPLEX GRADIENT

We list a few properties useful when deriving the complex gradient of real-valued functions of complex variables $\mathsf{z} \in \mathbb{C}^N$:

$$\tilde{\nabla}(c\, f(\mathsf{z})) = c\, \tilde{\nabla} f(\mathsf{z}) \tag{112a}$$

$$\tilde{\nabla}(f(\mathsf{z}) g(\mathsf{z})) = f(\mathsf{z}) \tilde{\nabla} g(\mathsf{z}) + g(\mathsf{z}) \tilde{\nabla} f(\mathsf{z}) \tag{112b}$$

$$\tilde{\nabla} h(f(\mathsf{z})) = \frac{\partial h}{\partial f} \tilde{\nabla} f(\mathsf{z}) + \frac{\partial h}{\partial f^*} \tilde{\nabla} f^*(\mathsf{z}) \tag{112c}$$

where $c \in \mathbb{C}$, $f, g : \mathbb{C}^N \to \mathbb{C}$, and $h : \mathbb{C} \to \mathbb{C}$.

By using the definition (73) and properties (112a)—(112c), one can derive the complex gradient for terms that are encountered in the expression of cost functions,

$$\tilde{\nabla}(\mathsf{z}^{\mathsf{H}}\mathsf{a}) = \tilde{\nabla}(\mathsf{a}^{\mathsf{T}}\mathsf{z}^*) = \mathsf{a} \tag{113a}$$

$$\tilde{\nabla}(\mathsf{a}^{\mathsf{H}}\mathsf{z}) = \tilde{\nabla}(\mathsf{z}^{\mathsf{T}}\mathsf{a}) = 0 \tag{113b}$$

$$\tilde{\nabla}\left(\mathsf{z}^{\mathsf{H}}\mathbf{\mathsf{M}}\mathsf{z}\right) = \mathbf{\mathsf{M}}\mathsf{z} \tag{113c}$$

$$\tilde{\nabla} \left|f(\mathsf{z})\right|^2 = f^*(\mathsf{z}) \tilde{\nabla} f(\mathsf{z}) + f(\mathsf{z}) \tilde{\nabla} f^*(\mathsf{z}) \tag{113d}$$

$$\tilde{\nabla} \operatorname{Re} f(\mathsf{z}) = \frac{1}{2}\big(\tilde{\nabla} f(\mathsf{z}) + \tilde{\nabla} f^*(\mathsf{z})\big) \tag{113e}$$

$$\tilde{\nabla} \operatorname{Im} f(\mathsf{z}) = \frac{1}{2\mathsf{j}}\big(\tilde{\nabla} f(\mathsf{z}) - \tilde{\nabla} f^*(\mathsf{z})\big) \tag{113f}$$

where $\mathsf{a} \in \mathbb{C}^N$ and $\mathbf{\mathsf{M}} \in \mathbb{C}^{N \times N}$.

APPENDIX C
STATIONARY EXPRESSION OF IMPEDANCE

Here, we determine the impedance coefficients z_i via a stationary (variational) expression. We directly minimize the norm of the error in the defining EFIE-IBC equation,

$$\mathsf{z}^\star = \underset{\mathsf{z} \,\in\, \mathbb{C}^L}{\arg\min} \left\| \boldsymbol{E}_{\tan} - Z(\mathsf{z}) \boldsymbol{J} \right\|^2 , \tag{114}$$

where

$$\boldsymbol{E}_{\tan}(\mathsf{I}) = \left[\boldsymbol{E}_{\mathrm{inc}} + \mathcal{L}\boldsymbol{J}\right]_{\tan} . \tag{115}$$

We observe that the cells $\mathcal{S}_i$ have non overlapping support, so that

$$\left\|\cdot\right\|^2 = \sum_{i=1}^{N_{\mathrm{c}}} \left\|\cdot\right\|^2_{\mathcal{S}_i} \tag{116}$$

where $\left\|\cdot\right\|^2_{\mathcal{S}_i}$ indicates integration over the support of cell i. We further note that with the choice of pulse basis functions (104) for $Z(\boldsymbol{r})$, a single z_i is involved in each cell, which simplifies the minimization instance (114) into a system of decoupled cell-wise minimization problems:

$$z_i^\star = \underset{z_i \,\in\, \mathbb{C}}{\arg\min} \left\| \boldsymbol{E}_{\tan} - z_i \boldsymbol{J} \right\|^2_{\mathcal{S}_i} , \quad \forall i = 1, ..., N_{\mathrm{c}} \tag{117}$$

The optimum is found by setting to zero the derivative of the norm in (117) with respect to z_i, which yields

$$z_i^\star = \frac{\langle\, \boldsymbol{E}_{\tan} \,, \boldsymbol{J}^* \,\rangle_{\mathcal{S}_i}}{\left\|\boldsymbol{J}\right\|^2} = \frac{\mathsf{I}^{\mathsf{H}} \mathbf{\Gamma}_i \mathsf{V}}{\mathsf{I}^{\mathsf{H}} \mathbf{\Gamma}_i \mathsf{I}} \tag{118}$$

where $\langle\, \cdot \,, \cdot \,\rangle_{\mathcal{S}_i}$ indicates integration over $\mathcal{S}_i$, and $\mathbf{\Gamma}_i \in \mathbb{R}^{N \times N}$ is the local Gram matrix (56) for the i-th cell. It is seen from the second derivative that this stationary point corresponds to a minimum.

REFERENCES

[1] Y. Liu, X. Liu, X. Mu, T. Hou, J. Xu, M. Di Renzo, and N. Al-Dhahir, "Reconfigurable Intelligent Surfaces: Principles and Opportunities," *IEEE Commun. Surv. Tutor.*, vol. 23, no. 3, pp. 1546–1577, 2021.

[2] G. Minatti, F. Caminita, M. Casaletti, and S. Maci, "Spiral Leaky-Wave Antennas Based on Modulated Surface Impedance," *IEEE Trans. Antennas Propag.*, vol. 59, no. 12, pp. 4436–4444, Dec. 2011.

[3] G. Minatti, F. Caminita, E. Martini, M. Sabbadini, and S. Maci, "Synthesis of Modulated-Metasurface Antennas With Amplitude, Phase, and Polarization Control," *IEEE Trans. Antennas Propag.*, vol. 64, no. 9, pp. 3907–3919, Sep. 2016.

[4] A. M. Patel and A. Grbic, "Effective Surface Impedance of a Printed-Circuit Tensor Impedance Surface (PCTIS)," *IEEE Trans. Microw. Theory Tech.*, vol. 61, no. 4, pp. 1403–1413, Apr. 2013.

[5] A. M. Patel and A. Grbic, "Modeling and Analysis of Printed-Circuit Tensor Impedance Surfaces," *IEEE Trans. Antennas Propag.*, vol. 61, no. 1, pp. 211–220, Jan. 2013.

[6] V. Sozio, E. Martini, F. Caminita, P. De Vita, M. Faenzi, A. Giacomini, M. Sabbadini, S. Maci, and G. Vecchi, "Design and Realization of a Low Cross-Polarization Conical Horn With Thin Metasurface Walls," *IEEE Trans. Antennas Propag.*, vol. 68, no. 5, pp. 3477–3486, May 2020.

[7] G. Minatti, M. Faenzi, E. Martini, F. Caminita, P. De Vita, D. González-Ovejero, M. Sabbadini, and S. Maci, "Modulated Metasurface Antennas for Space: Synthesis, Analysis and Realizations," *IEEE Trans. Antennas Propag.*, vol. 63, no. 4, pp. 1288–1300, Apr. 2015.

[8] S. Pearson and S. V. Hum, "Optimization of Electromagnetic Metasurface Parameters Satisfying Far-Field Criteria," *IEEE Trans. Antennas Propag.*, pp. 1–1, 2021.

[9] T. Brown, Y. Vahabzadeh, C. Caloz, and P. Mojabi, "Electromagnetic Inversion With Local Power Conservation for Metasurface Design," *IEEE Antennas Wirel. Propag. Lett.*, vol. 19, no. 8, pp. 1291–1295, Aug. 2020.

[10] T. Brown and P. Mojabi, "Cascaded Metasurface Design Using Electromagnetic Inversion With Gradient-Based Optimization," *IEEE Trans. Antennas Propag.*, vol. 70, no. 3, pp. 2033–2045, Mar. 2022.

[11] C. Narendra, T. Brown, and P. Mojabi, "Gradient-Based Electromagnetic Inversion for Metasurface Design Using Circuit Models," *IEEE Trans. Antennas Propag.*, vol. 70, no. 3, pp. 2046–2058, Mar. 2022.

[12] R. Palmeri, M. T. Bevacqua, A. F. Morabito, and T. Isernia, "Design of Artificial-Material-Based Antennas Using Inverse Scattering Techniques," *IEEE Trans. Antennas Propag.*, vol. 66, no. 12, pp. 7076–7090, Dec. 2018.

[13] J. Budhu, E. Michielssen, and A. Grbic, "The Design of Dual Band Stacked Metasurfaces Using Integral Equations," *IEEE Trans. Antennas Propag.*, pp. 1–1, 2022.

[14] J. Budhu and A. Grbic, "Perfectly Reflecting Metasurface Reflectarrays: Mutual Coupling Modeling Between Unique Elements Through Homogenization," *IEEE Trans. Antennas Propag.*, vol. 69, no. 1, pp. 122–134, Jan. 2021.

[15] M. Di Renzo, F. H. Danufane, and S. Tretyakov, "Communication Models for Reconfigurable Intelligent Surfaces: From Surface Electromagnetics to Wireless Networks Optimization," Oct. 2021.

[16] M. Bodehou, C. Craeye, E. Martini, and I. Huynen, "A Quasi-Direct Method for the Surface Impedance Design of Modulated Metasurface Antennas," *IEEE Trans. Antennas Propag.*, vol. 67, no. 1, pp. 24–36, Jan. 2019.

[17] M. Bodehou, C. Craeye, and I. Huynen, "Electric Field Integral Equation-Based Synthesis of Elliptical-Domain Metasurface Antennas," *IEEE Trans. Antennas Propag.*, vol. 67, no. 2, pp. 1270–1274, Feb. 2019.

[18] M. Bodehou, D. González-Ovejero, C. Craeye, S. Maci, I. Huynen, and E. Martini, "Power balance and efficiency of metasurface antennas," *Sci. Rep.*, vol. 10, no. 1, p. 17508, Oct. 2020.

[19] M. Bodehou and C. Craeye, "Array Surface-Wave Launcher for the Efficient Generation of Shaped Beam and Multibeam With Metasurface," *IEEE Trans. Antennas Propag.*, vol. 69, no. 12, pp. 8860–8865, Dec. 2021.

[20] G. Oliveri, P. Rocca, M. Salucci, and A. Massa, "Holographic Smart EM Skins for Advanced Beam Power Shaping in Next Generation Wireless Environments," *IEEE J. Multiscale Multiphysics Comput. Tech.*, vol. 6, pp. 171–182, 2021.

[21] M. Salucci, A. Gelmini, G. Oliveri, N. Anselmi, and A. Massa, "Synthesis of Shaped Beam Reflectarrays With Constrained Geometry by Exploiting Nonradiating Surface Currents," *IEEE Trans. Antennas Propag.*, vol. 66, no. 11, pp. 5805–5817, Nov. 2018.

[22] B. B. Tierney and A. Grbic, “Designing Anisotropic, Inhomogeneous Metamaterial Devices Through Optimization,” *IEEE Trans. Antennas Propag.*, vol. 67, no. 2, pp. 998–1009, Feb. 2019.

[23] L. Szymanski, G. Gok, and A. Grbic, “Inverse Design of Multi-Input Multi-Output 2-D Metastructured Devices,” *IEEE Trans. Antennas Propag.*, vol. 70, no. 5, pp. 3495–3505, May 2022.

[24] F. Caminita, E. Martini, G. Minatti, M. Sabbadini, and S. Maci, “Low-Profile Dual-Polarized Isoflux Antennas for Space Applications,” *IEEE Trans. Antennas Propag.*, vol. 69, no. 6, pp. 3204–3213, Jun. 2021.

[25] F. Vernì, “Advanced Computational Electromagnetics for Metasurfaces,” Ph.D. dissertation, Politecnico di Torino, Aug. 2020. [Online]. Available: https://iris.polito.it/handle/11583/2843986?mode=simple.13517

[26] F. Vernì, M. Righero, and G. Vecchi, “On the Use of Entire-Domain Basis Functions and Fast Factorizations for the Design of Modulated Metasurface,” *IEEE Trans. Antennas Propag.*, vol. 68, no. 5, pp. 3824–3833, May 2020.

[27] S. Koziel, M. Abdullah, and S. Szczepanski, “Design of High-Performance Scattering Metasurfaces Through Optimization-Based Explicit RCS Reduction,” *IEEE Access*, vol. 9, pp. 113 077–113 088, 2021.

[28] A. Epstein and G. V. Eleftheriades, “Synthesis of Passive Lossless Metasurfaces Using Auxiliary Fields for Reflectionless Beam Splitting and Perfect Reflection,” *Phys. Rev. Lett.*, vol. 117, no. 25, p. 256103, Dec. 2016.

[29] V. G. Ataloglou and G. V. Eleftheriades, “Arbitrary Wave Transformations With Huygens’ Metasurfaces Through Surface-Wave Optimization,” *IEEE Antennas Wirel. Propag. Lett.*, vol. 20, no. 9, pp. 1750–1754, Sep. 2021.

[30] G. Xu, V. G. Ataloglou, S. V. Hum, and G. V. Eleftheriades, “Extreme Beam-Forming With Impedance Metasurfaces Featuring Embedded Sources and Auxiliary Surface Wave Optimization,” *IEEE Access*, vol. 10, pp. 28 670–28 684, 2022.

[31] E. F. Kuester, M. A. Mohamed, M. Piket-May, and C. L. Holloway, “Averaged transition conditions for electromagnetic fields at a metafilm,” *IEEE Trans. Antennas Propag.*, vol. 51, no. 10, pp. 2641–2651, Oct. 2003.

[32] K. A. Michalski and J. R. Mosig, “Multilayered media Green’s functions in integral equation formulations,” *IEEE Trans. Antennas Propag.*, vol. 45, no. 3, pp. 508–519, Mar. 1997.

[33] M. A. Francavilla, E. Martini, S. Maci, and G. Vecchi, “On the Numerical Simulation of Metasurfaces With Impedance Boundary Condition Integral Equations,” *IEEE Trans. Antennas Propag.*, vol. 63, no. 5, pp. 2153–2161, May 2015.

[34] S. Rao, D. Wilton, and A. Glisson, “Electromagnetic scattering by surfaces of arbitrary shape,” *IEEE Trans. Antennas Propag.*, vol. 30, no. 3, pp. 409–418, May 1982.

[35] K. A. Michalski, “Electromagnetic Field Computation in Planar Multilayers,” in *Encyclopedia of RF and Microwave Engineering*. John Wiley & Sons, Ltd, 2005.

[36] W. C. Chew, J.-M. Jin, E. Michielssen, and J. Song, *Fast and Efficient Algorithms in Computational Electromagnetics*. Boston: Artech House, 2001.

[37] S. M. Seo and J.-F. Lee, “A fast IE-FFT algorithm for solving PEC scattering problems,” *IEEE Trans. Magn.*, vol. 41, no. 5, pp. 1476–1479, May 2005.

[38] Fasenfest, Capolino, Wilton, Jackson, and Champagne, “A fast MoM solution for large arrays: Green’s function interpolation with FFT,” *IEEE Antennas Wirel. Propag. Lett.*, vol. 3, pp. 161–164, 2004.

[39] J. Nocedal and S. J. Wright, *Numerical Optimization*, 2nd ed., ser. Springer Series in Operations Research. New York: Springer, 2006.

[40] “IEEE Standard for Definitions of Terms for Antennas,” *IEEE Std 145-2013 Revis. IEEE Std 145-1993*, pp. 1–50, Mar. 2014.

[41] D. H. Brandwood, “A complex gradient operator and its application in adaptive array theory,” *IEE Proc. F Commun. Radar Signal Process.*, vol. 130, no. 1, pp. 11–16, Feb. 1983.

[42] L. Teodorani, M. Zucchi, and G. Vecchi, “Numerically-Synthesized Broadside-Radiating Leaky-Wave Antenna,” in *2023 IEEE Int. Symp. Antennas Propag. USNC-URSI Radio Sci. Meet. AP-SURSI*, Jul. 2023, pp. 1–2.

[43] G. Minatti, E. Martini, and S. Maci, “Efficiency of Metasurface Antennas,” *IEEE Trans. Antennas Propag.*, vol. 65, no. 4, pp. 1532–1541, Apr. 2017.

[44] A. Arroyo, R. Contreres, A. Piche, H. Roussel, and M. Casaletti, “Linear Polarization from Scalar Modulated Metasurfaces,” in *2022 16th Eur. Conf. Antennas Propag. EuCAP*, Mar. 2022, pp. 1–4.

[45] D. González-Ovejero, N. Chahat, R. Sauleau, G. Chattopadhyay, S. Maci, and M. Ettorre, “Additive Manufactured Metal-Only Modulated Metasurface Antennas,” *IEEE Trans. Antennas Propag.*, vol. 66, no. 11, pp. 6106–6114, Nov. 2018.

[46] M. Zucchi, “Numerical Techniques for the Automated Design of Metasurface Antennas,” Ph.D. dissertation, Politecnico di Torino, Oct. 2022. [Online]. Available: https://iris.polito.it/handle/11583/2972560